UNIVERSITY OF CALIFORNIA
RIVERSIDE

Thermionic Cascade in Graphene-Boron Nitride Heterostructures

A Dissertation submitted in partial satisfaction
of the requirements for the degree of

Doctor of Philosophy

in

Physics

By

Jacky C. Wan

June 2022

Dissertation Committee:
Dr. Nathaniel Gabor, Chairperson
Dr. Yongtao Cui
Dr. Peng Wei

The Dissertation of Jacky C. Wan is approved:

_____

_____

_____

Committee Chairperson

University of California, Riverside

ACKNOLWEDGEMENTS

“I always tell people that you can call me anything that you want. […] But don’t ever ever call me a self-made man. That is so important for you to understand. I didn’t make it that far on my own.”

- Arnold Schwarzenegger

I would like to thank my advisor, Dr. Nathaniel M. Gabor, for his guidance and patience in working with me during my PhD program. I have learned much from his passion in research and also his broad range of interests which always seems to connect with one another.

I would like to thank Dr. Leonid S. Levitov, and Dr. Justin C. W. Song for their inspiring discussions on this project.

I would like to thank Dr. Yongtao Cui and Dr. Peng Wei for spending their time to serve on my committee.

I would like to thank all lab members of the QMO Lab from whom I have learned a great deal from and have made my graduate school experience much more enjoyable.

DEDICATION

To all those who I call my friends,

without whom I would not have decided to be here today.

To my closest friend in the department who is also my closest friend in all of Southern California, whose thoughtful conversations and consistent support have made it possible for me to be here.

ABSTRACT OF THE DISSERTATION

Thermionic Cascade in Graphene-Boron Nitride Heterostructures

BY

Jacky C. Wan

Doctor of Philosophy, Graduate Program in Physics
University of California, Riverside, June 2022
Dr. Nathaniel Gabor, Chairperson

We stack-engineer an optically gated thermionic valve which acts as a thermometer for hot electronic charge carriers. Through pulsed photoexcitation of encapsulated graphene-boron nitride-graphene heterostructure devices, we trigger picosecond charge carrier transit through an ultrathin BN barrier. The resultant interlayer photoconductance exhibits extraordinary enhancement near the charge neutrality (Dirac) point of graphene. We attribute this to ultrafast thermionic cascade arising from an elevated electronic temperature from the rapidly thermalizing electrons and holes. The electronic temperature was found to peak at the Dirac point and reaches well above 2000 K. This Dirac point thermionic cascade can also be dramatically quenched via electrical control at low temperatures, which indicates unconventional-yet highly efficient- cooling pathways that serve as a hallmark of Dirac electron-hole plasma in graphene.

TABLE OF CONTENTS

LIST OF FIGURES

LIST OF TABLES

CHAPTER 1

Introduction and Background

1.1 Introduction

Graphene has been a playground in condensed matter research for the past few decades owing to its novel electronic qualities. The two-dimensional (2-D) nature of graphene combined with its hexagonal symmetry gives rise to a Dirac cone in its electronic band structure [4,12] near the charge neutrality (Dirac) point. This Dirac cone implies a linear dispersion relation near charge neutrality, unlike in conventional materials. This linear dispersion relation give rise to the unique characteristics of Dirac Fermions. Although graphene is not the only material with this characteristic, it is one of the earliest to be discovered and remains the most straightforward to work with. Owing to the relative ease in isolating monolayer of graphene, it has been the material of choice for studying the unique characteristics of Dirac Fermions. Here, we aim to study the heating and cooling dynamics of charge carriers in photoexcited graphene. By generating electron-hole excited states from ultrafast pulse laser excitation, we assess how absorbed energy from light is taken and dissipated/transported via carrier-carrier interactions and their interactions with the environment.

1.2 Electron-Electron Interaction in Graphene

Unlike in most conventional metallic systems, charge carriers in graphene can interact much more strongly with each other owing to the linear dispersion of the Dirac

cone[3,7,10]. In a conventional metal, the dynamics of charge carriers are dominated by its kinetic energy at high densities, while interaction is only appreciable at low densities. This is due to the parabolic nature of the usual 2-D electronic energy bands. The Hamiltonian for interacting electrons in a conventional metal is (eq. 1.1)

$$H = \frac{\boldsymbol{P}^2}{2m} + \frac{e^2}{\varepsilon\varepsilon_0(\boldsymbol{r} - \boldsymbol{r}')} \tag{1.1}$$

where $\boldsymbol{P}$ is the momentum operator, m is the effective mass of the carrier, e is the electron charge, and $\boldsymbol{r}$ is the position of the carriers. The first term describes the kinetic energy of charge carriers and the latter describes the coulomb interaction. When calculating the average kinetic energy of charges carriers, E_K, we find that $E_K \sim n$, where n is the charge density of the system. When we perform the same calculation for the potential energy from the coulomb interaction, E_C, we find that $E_C \sim n^{1/2}$. This implies that the ratio of coulomb energy to kinetic energy is $E_C/E_K \sim n^{-1/2}$. Therefore, at high densities, kinetic energy dominates; interaction dominates only at extremely low densities. This suggests that interactions are negligible under most conditions.

On the other hand, due to the linear dispersion of the Dirac cone, the Hamiltonian is of the form (eq. 1.2)

$$H = \pm v_F|\boldsymbol{P}| + \frac{e^2}{\varepsilon\varepsilon_0(\boldsymbol{r} - \boldsymbol{r}')} \tag{1.2}$$

in which the kinetic energy term has a linear (rather than a parabolic) form, with v_F being the Fermi velocity in graphene. When we perform the same calculation as above, we find that both the E_C and E_K are proportional to $n^{1/2}$; thus their ratio depends only on material constants (eq. 1.3)

$$\frac{E_C}{E_K} \sim \frac{e^2}{\varepsilon\varepsilon_0 v_F \hbar} \tag{1.3}$$

where e is the electron charge, ε is the relative dielectric constant of the space surrounding the graphene, ε_0 is the vacuum permittivity, v_F is the fermi velocity, and $\hbar$ is the reduced Planck's constant. This suggests that the Coulomb interaction is only negligible if this ratio is much smaller than 1. Given that v_F in graphene is nominally 10^6 *m/s* this yields $\frac{E_C}{E_K}$ to be on the order of 1, which means interactions are not negligible, across the Dirac cone regardless of the doping level. This unique nature of a Dirac system (including graphene) presents a unique electronic landscape that opens the door for novel electronic states due to this strong interaction.

1.3 Quantum Critical Graphene

Charge carriers in graphene can be tuned into a strongly interacting regime thanks to the relatively strong carrier-carrier interactions. Although charge carriers in graphene have appreciable interaction strength compared to conventional systems, this interaction between carriers must still compete with interactions such as that with phonons and disorder. Regardless, this relatively strong carrier interaction offers the opportunity to tune graphene such that the carrier-carrier interaction is the dominant interaction in the system. This manifests as unique characteristics due to the collective behaviors of charge carriers in this regime. For example, it has been both theoretically predicted and experimentally shown that under the right conditions, charge carriers in graphene can behave as viscous liquid[1,8,11]. Moreover, there have been theoretical predictions that at charge neutrality and

zero temperature, graphene has a quantum critical point that supports the coexistence of strongly interacting holes and strongly interacting electrons. In this regime, electrons and holes form a charge neutral plasma known as a Dirac liquid[9]. Evidence of this Dirac liquid has been demonstrated recently in low temperature transport measurements. Due to the collective nature of electrons and holes, efficient hydrodynamic transport of this charge neutral plasma leads to the breakdown of Wiedemann-Franz Law in graphene at charge neutrality[5].

Rather than cooling a system to suppress the scattering with phonons and disorder we can tune the graphene into this Dirac Liquid phase by elevating its electronic temperature[10]. Normally, elevating the electronic temperature would be equivalent to elevating the lattice temperature since carriers and the lattice reaches equilibrium quickly. The consequence of this is that while the elevated electronic temperature helps drive the system into the Dirac liquid phase, the increase in lattice temperature leads to strong scattering with disorder, phonons, and other thermal effects that destroy the Dirac liquid phase. However, thanks to the strong coupling between carriers in graphene and the relatively weak coupling between carriers and the lattice, we can excite the carriers and not the lattice. Indeed, more recently, photoexcited graphene has shown promise in generating this Dirac electron-hole plasma [2,6]. Here we aim to utilize this photoexcitation scheme for elevating the electronic temperature thus driving graphene into the Dirac Liquid phase. We stack engineer a system that allows us to study the heating and cooling dynamics of the excited electrons and holes and measure the heating and cooling dynamics of this Dirac Liquid.

REFERENCES

[1] D. A. Bandurin, et al., Negative local resistance caused by viscous electron backflow in graphene, Science Vol. 351, issue 6277, 1055-1058 (2016)

[2] A. Block, et al., Observation of giant and tunable thermal diffusivity of a Dirac fluid at room temperature, Nature Nanotech. Vol 16 1195-1200, (2021)

[3] A. H. Castro Neto et al., The electronic properties of graphene, Rev. Mod. Phys., 81, 109 (2009).

[4] D. R. Cooper, B. D'Anjou, et al. Experimental Review of Graphene, *International Scholarly Research Notices*, vol. 2012

[5] J. Crossno, et al., Observation of the Dirac fluid and the breakdown of the Wiedemann-Franz law in graphene, Science, Vol. 351, issue 6277, 1058-1061 (2016)

[6] P. Gallagher, et al., Quantum-critical conductivity of the Dirac fluid in graphene Science, vol 364, issue 6436, 158-162, (2019)

[7] V. N. Kotov, Bruno Uchoa, Vitor M. Pereira, F. Guinea, and A. H. Castro Neto, Electron-Electron Interactions in Graphene: Current Status and Perspectives, Rev. Mod. Phys. 84, 1067 (2012)

[8] L. Levitov, G. Falkovich, Electron viscosity, current vortices and negative nonlocal resistance in graphene, *Nature Physics*, **12**, pages672–676 (2016)

[9] D. E. Sheehy, et al., Daniel E. Sheehy, et al., PhysRevLett,99,226803 (2007), PhysRevLett,99,226803 (2007)

[10] D. E. Sheehy, and Jörg Schmalian, Quantum Critical Scaling in Graphene, PRL **99,** 226803 (2007)

[11] J. A. Sulpizio, L. Ella, A. Rozen, John Birkbeck, et. al., Visualizing Poiseuille Flow of Hydrodynamic Electrons, *Nature* **576,** 75–79 (2019)

[12] P. R.Wallace, "The band theory of graphite," *Physical Review*, vol. 71, no. 9, pp. 622–634 (1947)

CHAPTER 2

Hot Carriers in Graphene and Graphene Thermometer Design

2.1 Introduction

Photoexcited carriers in graphene rapidly form a thermalized hot distribution[4,16]. This unique characteristic originates from the strong carrier-carrier interactions and the linear dispersion of the Dirac cone in graphene. Owing to the relatively weak coupling between the atomic lattice and the charge carriers, the temperature of these hot carriers can be orders of magnitude larger than the lattice temperature and is relatively long lived. This provides the opportunity to use optoelectronic probes to study the heating and cooling dynamics of both the electron-hole excited state and the predicted Dirac electron-hole plasma. To do so, devices using graphene must be designed based on the evolution of these hot carriers, particularly their thermalization process, in order to extract a measurable photoresponse.

2.2 Hot Carrier Evolution in Graphene

Immediately after photoexcitation, the photon energy is divided between a population of electrons and holes (Fig 2.1a). Thanks to the linear dispersion of the Dirac cone, electrons and holes then scatter with each other via elastic, momentum-conserving Auger-like processes (Fig 2.1b). Within approximately 100 *fs*, the initial population of electrons and holes would have completely thermalized into a hot Fermi-Dirac distribution of carriers with an elevated temperature from the lattice temperature [2,3,7,9,15] (Fig 2.1c).

Once this quasi-thermal equilibrium is established, the hot carriers, by coupling to phonons, begin to relax over the next few tens of picoseconds[1,5,6,7,9]. Initially, the hot distribution loses part of its energy by coupling to optical phonons (Fig. 2.1d). This occurs extremely quickly, and the distribution can cool significantly over a few tens of femtoseconds. However, these optical phonons must decay into lower energy acoustic phonons before the hot distribution can cool (once again via optical phonons[11]) (Fig. 2.1e). During this time, the remaining hot carriers re-thermalize into a new hot distribution. This process of cooling and rethermalizing continues until the hot carrier distributions have equilibrated with the lattice. Although the coupling to optical phonons is fast, this phonon bottle neck allows the quasi-thermal equilibrium to persist on the order of picoseconds, which is long enough for us to probe the dynamics of this hot distribution using ultrafast techniques.

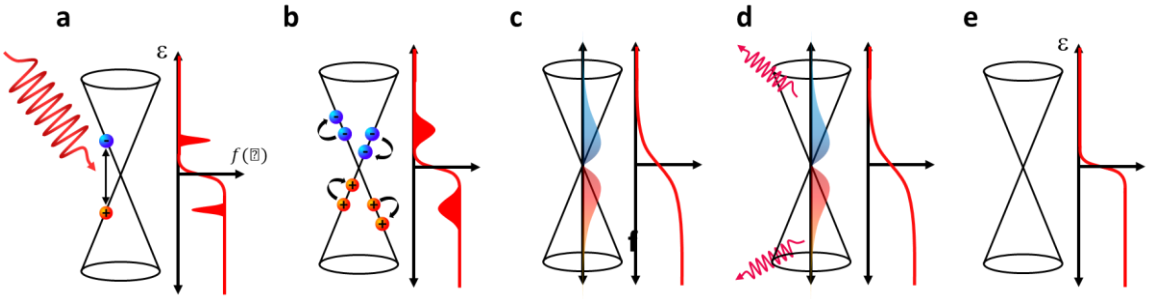

Figure 2.1 Lifetime of Photoexcited Carriers in Graphene (a) Initial Excitation (b) Auger processes and carrier-carrier interactions (c) quasi-thermal equilibrium established over a 100 *fs* (d) cooling by optical then acoustic phonons. (e) Return to equilibrium.

2.3 G/hBN/G Heterostructure Design (Graphene Thermometer)

The hot carriers generated in graphene under photoexcitation can be extracted and probed to determine an effective electronic temperature. Changes in this electronic temperature will indicate changes in hot carrier relaxation pathways in graphene as a function of lattice temperature, charge density, and crystal quality. In designing a heterostructure that provides a useful photoresponse for extracting the electronic temperature, we look to a conventional thermometer as inspiration. In a conventional thermometer, a glass-encased medium (e.g., liquid mercury) absorbs heat from its environment and expands. This causes the level of the medium to increase in height. Thus the temperature can be determined by height reached by the medium. We can apply a similar concept to charge carriers in graphene, in which the medium is now the charge carriers.

When the charge carriers in graphene absorb energy, they thermalize as described in the previous section. Within a thermalized distribution, many charge carriers will reach a higher energy than the initial excited population. The hotter the thermalized distribution, the more carriers will reach energies that are higher than the initial excitation. By introducing an out-of-plane energy barrier we can filter out the high energy tail of this distribution[10,12,13,14,17] and extract them as a photocurrent. The magnitude of this photocurrent is directly related to the number of carriers with high enough energy to overcome the energy barrier which can then be related to the electronic temperature of this system. We create our graphene thermometer with two layers of graphene separated by thin layer of hexagonal boron nitride, which acts as our energy barrier.

The devices studied here, and described in the following chapters, are high-mobility monolayer graphene/hBN/graphene heterostructures (Fig. 2.3). These devices consist of two spatially overlapping graphene sheets, labeled G_T and G_B (top and bottom respectively), separated by a thin hexagonal boron nitride (hBN) layer. By using hBN layers with thickness L = 7-10nm. This hBN thickness fully suppresses the G-hBN-G tunneling[2] and photon assisted-tunneling current[8] at low voltages, and ensures the photoresponse is dominated by transport of hot carriers. The constituent layers, including the hBN encapsulants, were mechanically laminated via an inverted dry transfer method using polymer stamps (see Section 3).

Here in Chapter 2, we have discussed the evolution of photoexcited charge carriers and the design and operating principles behind our intended device to be studied. In Chapter 3 we describe the details of device fabrication before describing their photoresponses. This includes preparations of substrates for exfoliation and integration into measurements, methods for isolating individual graphene and hBN flakes, and advances in fabrication techniques for efficient device fabrication.

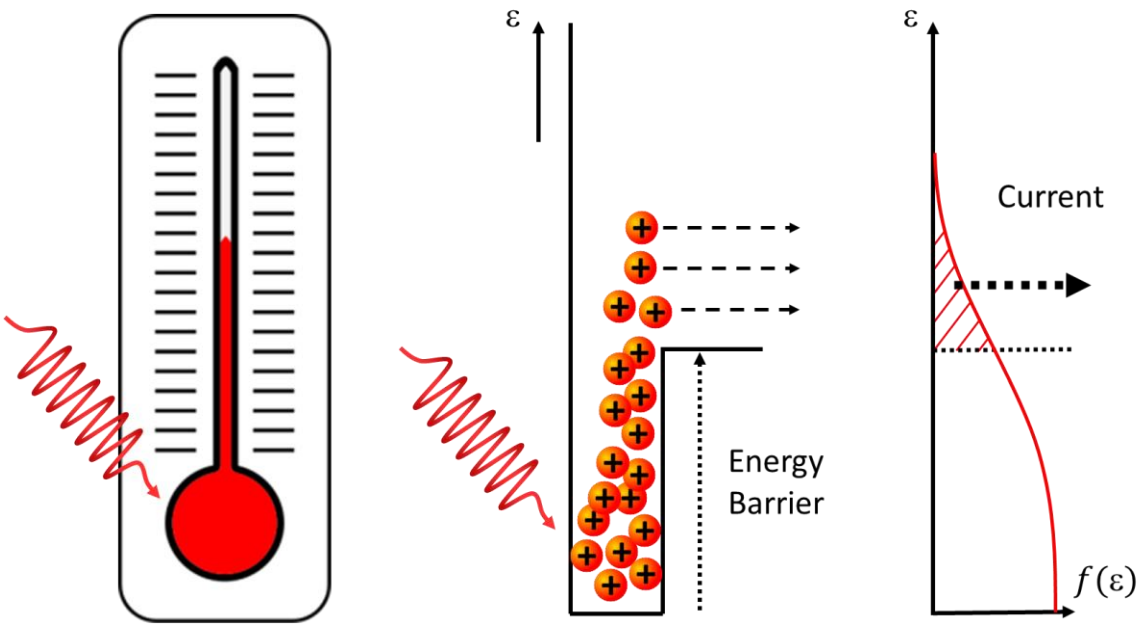

Figure 2.2 Graphene Thermometer. A schematic of a conventional thermometer in comparison to a graphene thermometer in which charge carriers forms the medium which is being heated.

REFERENCES

[1]. A. Betz, S. Jhang, E. Pallecchi, et al. Supercollision cooling in undoped graphene. *Nature Phys* **9**, 109–112 (2013).

[2] L. Britnell, et al. Electron Tunneling through Ultrathin Boron Nitride Crystalline Barriers, *Nano Lett.* 12, 3, 1707–1710 (2012)

[3] C. Ferrante, A. Virga, L. Benfatto, M. Martinati, D. De Fazio, U. Sassi, C. Fasolato, A. K. Ott, P. Postorino, D. Yoon, G. Cerullo, F. Mauri, A. C. Ferrari, T. Scopigno. Raman spectroscopy of graphene under ultrafast laser excitation. *Nat. Commun.* **9**, 308 (2018).

[4] I. Gierz, J. Petersen, M. Mitrano, C. Cacho, I. C. Edmond Turcu, E. Springate, A. Stöhr, A. Köhler, U. Starke and A. Cavalleri Snapshots of non-equilibrium Dirac carrier distributions in graphene. *Nature Mater* **12,** 1119–1124 (2013).

[5] M. Graham, S. Shi, D. Ralph, et al. Photocurrent measurements of supercollision cooling in graphene. *Nature Phys.* **9**, 103–108 (2013).

[6] M. W. Graham, S. Shi, Z. Wang, D. C. Ralph, J. Park, P. L. McEuen. Transient Absorption and Photocurrent Microscopy Show That Hot Electron Supercollisions Describe the Rate-Limiting Relaxation Step in Graphene. *Nano Lett.* **13**, 11, 5497–5502 (2013).

[7] J. C. Johannsen et al. Direct View of Hot Carrier Dynamics in Graphene. *Phys. Rev. Lett.* **111**, 027403 (2013).

[8] A Kuzmina, M. Parzefall, P. Back, T. Taniguchi, K. Watanabe, A. Jain, L. Novotny. Resonant Light Emission from Graphene/Hexagonal Boron Nitride/ Graphene Tunnel Junctions. *Nano Lett.* 21, 19, 8332–8339 (2021)

[9] Q. Ma, N. M. Gabor, T. I. Andersen, N. L. Nair, K. Watanabe, T. Taniguchi, P. Jarillo-Herrero. Competing Channels for Hot-Electron Cooling in Graphene. *Phys. Rev. Lett.* **112**, 247401 (2014).

[10] M. Massicotte, P. Schmidt, F. Vialla, *et al.* Photo-thermionic effect in vertical graphene heterostructures. *Nat Commun* **7,** 12174 (2016)

[11] E. A. A. Pogna, X. Jia, Hot-Carrier Cooling in High-Quality Graphene Is Intrinsically Limited by Optical Phonons, *ACS Nano*, 15, 7, 11285–11295 (2021)

[12] J. F. Rodriguez-Nieva, M. S. Dresselhaus, and J. C. W. Song, Enhanced Thermionic-Dominated Photoresponse in Graphene Schottky Junctions

[13] D. Sinha and J. U. Lee, Ideal Graphene/Silicon Schottky Junction Diodes, *Nano Lett.* 2014, 14, 8, 4660–4664

[14] K. J. Tielrooij, et al. Generation of photovoltage in graphene on a femtosecond timescale through efficient carrier heating. *Nature Nanotech.* **10**, 437–443 (2015).

[15] A. Tomadin, D. Brida, G. Cerullo, A. C. Ferrari, M. Polini. Nonequilibrium dynamics of photoexcited electrons in graphene: Collinear scattering, Auger processes, and the impact of screening. *Phys. Rev. B* **88**, 035430 (2013).

[16] A. Tomadin, S. M. Hornett, The ultrafast dynamics and conductivity of photoexcited graphene at different Fermi energies.

[17] M. Trushin, Theory of thermionic emission from a two-dimensional conductor and its application to a graphene-semiconductor Schottky junction, Appl. Phys. Lett. 112, 171109 (2018)

CHAPTER 3

Graphene/hBN/Graphene Heterostructure Fabrication

3.1 Introduction

Device fabrication is a core challenge in all measurements involving graphene and other atomic layer materials. While the 2D nature of atomic layer materials opens new prospects for studying novel mechanical and electronic properties[3], this lowered dimensionality also poses a practical limit on the size and quality of samples that can be achieved in a laboratory setting. Thus, a wealth of techniques and improvements must be made to create the desired system for study.

The study of the majority of atomic layer materials, not only graphene, requires the creation of a heterostructure. These heterostructures consist of individually isolated flakes of desired materials which are mechanically laminated on top of each other into a stack. The function of these heterostructures is 1) to combine the electronic properties of neighboring materials to create a playground for emergent and novel physical properties and 2) to encapsulate and protect the material being studied from its ambient environment. To achieve these goals, careful manipulation of individual small flakes of materials is required; simultaneously, interfaces must be kept clean during the fabrication process. Below I lay out the methods and techniques for how we create the graphene thermometer described in the previous section for studying the heating and cooling dynamics of electron-hole excited states. The final heterostructure for the devices studied here are either hBN/Graphene/hBN/Graphene/hBN or hBN/Graphene/hBN/Graphene/SiO_2; in these

heterostructures, the Graphene/hBN/Graphene thermometer is encapsulated between two layers of hBN or by a single layer of hBN and the substrate.

3.2 Wafer Preparation

The foundation of any heterostructure is the substrate. The cleanliness and choice of material is important to the final quality of the heterostructure which will go on it. The wafers are used both for isolating the individual layer of materials and for carrying the final Graphene-hBN-Graphene heterostructures. A process of cleaning and prepatterning is done to maintain the quality of our samples and for easy identification respectively.

The Graphene-hBN-Graphene heterostructures are fabricated on common Si/SiO_2 substrates. We utilize wafers that are 2 inches in diameter that have an oxide layer of approximately 280nm +/-5% in thickness with a (100) crystal orientation on the surface (Fig. 3.1). This oxide layer thickness provides a good optical contrast for optically identifying a range of thicknesses from ultra-thin to monolayer in both graphene and hexagonal boron nitride; additionally, the crystal orientation provides the best yield on number and size of the individual flakes during the exfoliation process described in the next section.

Figure 3.1 Sample Wafers for Fabrication. (Left) New unpatterned wafer. (Right) Patterned wafer ready for use.

On average, the flakes of the individual materials which will be useful for creating a heterostructures are on the order of only tens of microns (Fig 3.2). Due to the relatively small size of these flakes, we prepattern our silicon substrate with identifying marks such that we can record the locations of useful flakes and easily locate them during the entire fabrication process. We pattern our silicon substrate using photolithography and ion etching in a cleanroom environment. We first spin coats a layer of HMDS polymer on top of our silicon wafers which acts as an adhesion layer for the photoresist. We spin coat at 4000 rpm for 40 s with a ramp up and ramp down speed of 1000 rpm/s. Next, we spin coat a 5214 photoresist on top of our HMDS layer with the same spin coating settings as described above. The photoresist is then cured on a hotplate at 110℃ for 5 minutes. Once

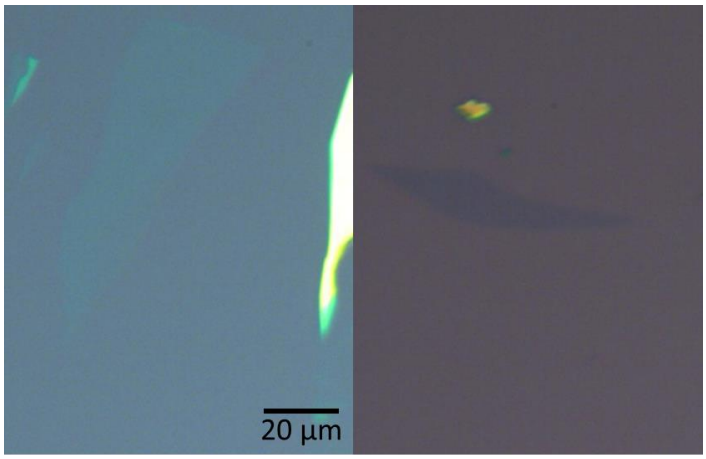

Figure 3.2 Exfoliated Flakes Examples. Samples of a usable piece of hBN flake (Left) and Graphene flake (Right)

the photoresist is set, the wafer is then transferred on to the stage of a Karl Suss Mask Aligner. A custom-made photomask with a pattern of arrows and crosses is then center-aligned on our wafer for exposure. An ultraviolet light is exposed through the mask for 16

seconds. The pattern is then developed in a solution of AZ 400K developer and deionized water in a 1:4 ratio. Once developed, the photoresist in the areas exposed to the ultraviolet light is removed, thus exposing the wafer underneath. The wafer is then taken to a Reactive Ion Etch station in which it is etched using CH_4 and CH_3F gases for 2 minutes. This process etches away part of the surface SiO_2 thus leaving behind visible marks on the surface.

After prepatterning, the surface of the wafer must be cleaned to protect our graphene and hBN layers from surface contaminants. We first remove the remaining photoresist which has hardened onto the surface of the wafer after the etching. This is done with an acetone sprayer which removes most of the remaining photoresists. The wafer is then cut into smaller pieces of approximately 5 mm x 5 mm in size. The wafer pieces are then transferred into a beaker of acetone and sonicated for 15 minutes. Afterwards, they are rinsed off with isopropyl alcohol and dried using compressed nitrogen gas. After drying, the wafer pieces are ready for use as substrates.

3.3 Exfoliation

We isolate the individual layers of materials needed for the final graphene-hBN-Graphene heterostructure via mechanical exfoliation. Below I will describe the techniques used in this process and improvements made which includes a standard manual exfoliation process, along with a mechanized exfoliation process to assist in more consistent and higher throughput results. The aim in this process is to improve the probability of obtaining uniform large area flakes with the correct thickness.

Our manual exfoliation technique is based on those previous reported in literature[2]. To obtain graphene, we start with a bulk piece of Kish Graphite on a piece of Scotch Magic tape, while, for hBN, we start with either a bulk crystal of hBN or an hBN powder on a piece of tape. The piece of tape is then folded in half such that both sides of the bulk crystal are in contact with the tape. We then peel apart the tape in a smooth and consistent manner thus cleaving the bulk crystal. This process is repeated until the crystal has spread out over a large area on the tape (Fig. 3.3).

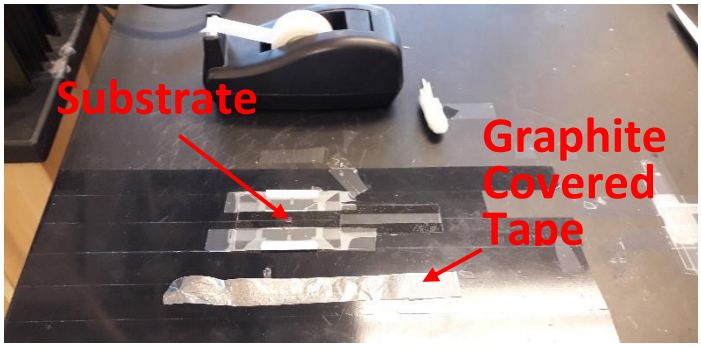

Figure 3.3 Materials for Exfoliation. A piece of tape covered in the peeled bulk crystal of choice (bottom) is ready to be placed in contact with the purple silicon substrate on the exfoliation.

Once the tape with the crystals is prepared, we take one of the previously cleaned and patterned substrates and secure it onto our work surface with a piece of double-sided carbon tape. The crystal covered tape is then laid down onto the substrate such that the crystals are now in contact with the substrate's surface. A cotton swab is used to gently press down to create full contact between the substrate's surface and crystals on the surface of the tape. The tape is then peeled off by elevating one side of the tape or by folding the tape over and pulling along the length of the tape (Fig. 3.4).

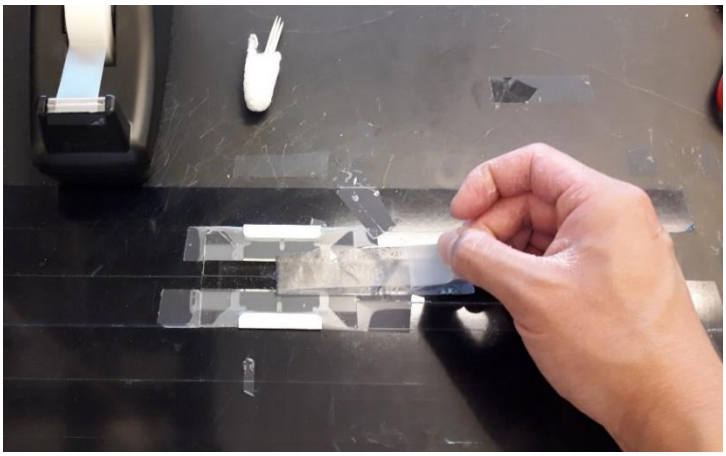

Figure 3.4 Exfoliation by Peeling. Tape is peeled off in a smooth and steady manner to leave behind ultrathin flakes of the desired material.

The latter method appears to be more effective; it utilizes the natural curvature of the tape to dictate the peeling angle; this method also affords easier control of the speed of the peeling action which is most effective when it is approximately 1mm/s or less. Once the tape has been peeled away from the substrate's surface, the substrate is then taken to an inspection microscope where the useful flakes are identified.

Over the years, the application of automated machines along with heating techniques has improved upon the manual exfoliation technique. One of the greatest challenges in exfoliation is the manual aspect of the process. Fatigue of the researcher often affects how many wafers a person can process at one time, and natural muscle inconsistency leads to poor control of the speed at which the tape is peeled off the surface of a substrate. These factors lead to low volume and low quality of useful flakes. Here we attempt to remedy these problems by constructing simple yet effective robotic machines to replace the human hand (Fig. 3.5); we also add a heating scheme that produces better flakes.

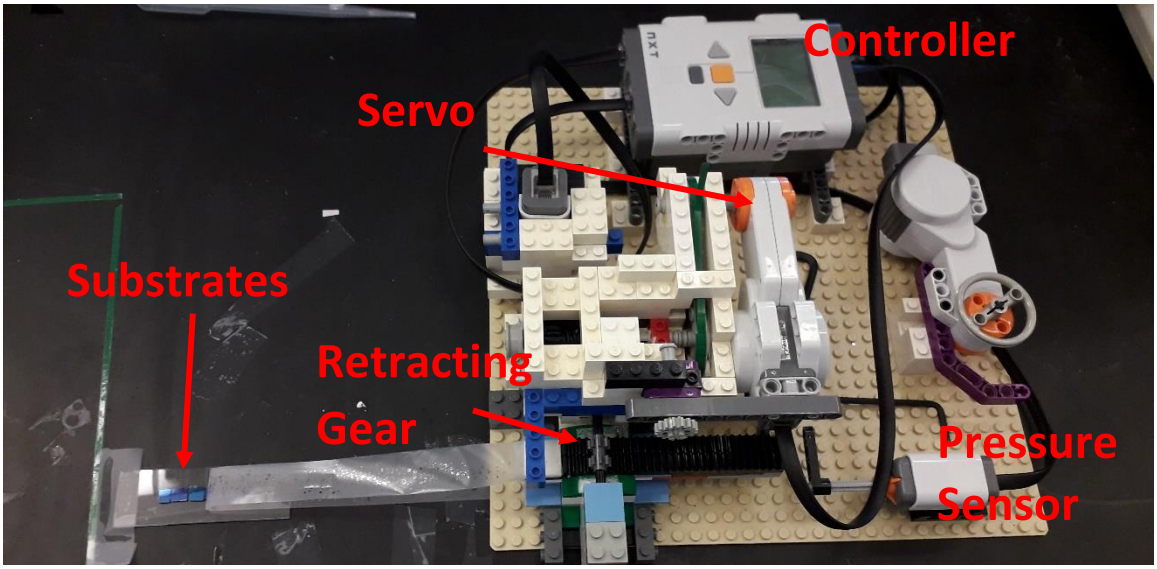

Figure 3.5 Mechanical Exfoliation Machine. A LEGO machine built to peel the crystal covered tape in a more controlled and consistent manner; it also process a larger array of wafers compared to the manual exfoliation.

The machine shown here is built using LEGO and a LEGO robotics system controller. The controller powers a servo motor which rotates a gear to retract a beam to which the tape is attached. This mechanism actuates the peeling motion of the tape and the speed of this motion has been programed to be adjusted by turning the wheel on the right. A pressure sensor is placed at the right side of the beam such that it will stop automatically when the peeling is complete. This machine allows us to prepare multiple substrates at the same time, thus improving efficiency.

In this new process, a heating step is added for better contact of the material covered tape and the substrates. The preparation of the 2D material covered tape is the same as the as the manual process. After we lay the tape on top of the array of substrates, the substrates are then heated on a hotplate at 60℃ for 60 seconds while a weight is placed on top of the

tape to promote surface contact between the material and the substrate. The substrate, with the tape still on it, is then removed from the hotplate and allowed to be cooled back to room temperature before attaching it to the machine to have the tape peeled off. This process yields a significant improvement in the number of flakes of a quality that makes them useful for creating graphene devices.

3.4 Flake Characterization

Both hBN and Graphene flakes that are exfoliated needs to be characterized to confirm their thickness. Our aim is to isolate monolayer graphene and hBN of thickness near 10 nm. Monolayer graphene and thin hBN are first identified optically under a trained eye, and verified using Raman spectroscopy and Atomic Force Microscopy respectively.

The thickness of our graphene layer is determined using a HORIBA RAMAN system using a 532nm illumination. The resulting Raman spectra show two main Raman modes of interest, the so called 2D and G bands. The 2D band corresponds to one of the in-plane breathing modes of graphene, while the G band corresponds to one of the in-plane vibrational modes. In monolayer graphene, the 2D band Raman intensity is significantly stronger than the G band [4,5]. We can determine if the graphene flake is monolayer by plotting the Raman spectra and comparing the intensity of the 2D peak and G peak (Fig. 3.6). The thickness of the hBN layer separating the two graphene layers was determined using an AFM system (Fig 3.7). This step is generally done after the device has been measured to preserve the cleanliness of the hBN layer and to prevent accidental damage to the layer. The thickness of our hBN layers is between 7 and 10 nm (Table 3.1).

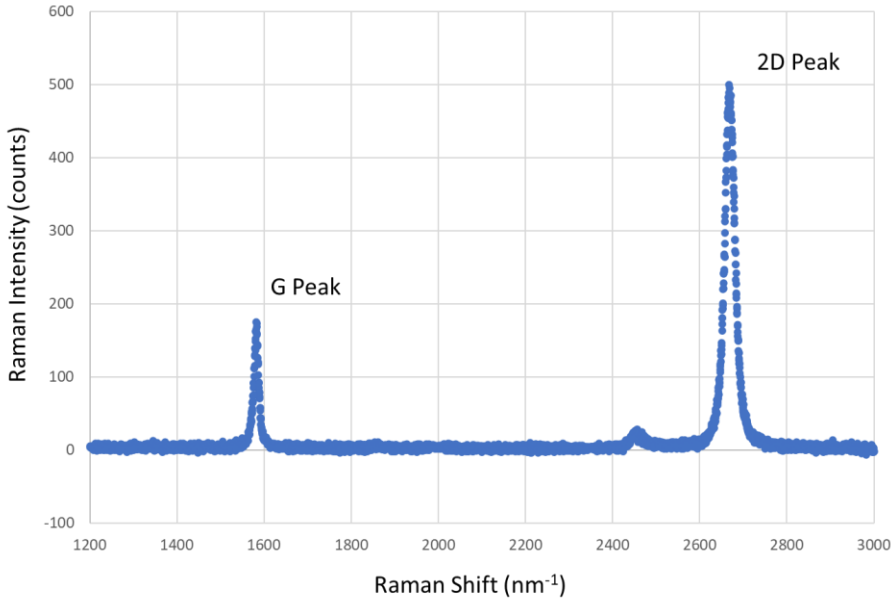

Figure 3.6 Monolayer Graphene Raman Spectra. The Raman intensity plotted as a function of the Raman shift shows the 2D and G Peaks in graphene's Raman spectra. In monolayer graphene, the 2D Peak is stronger than the G Peak.

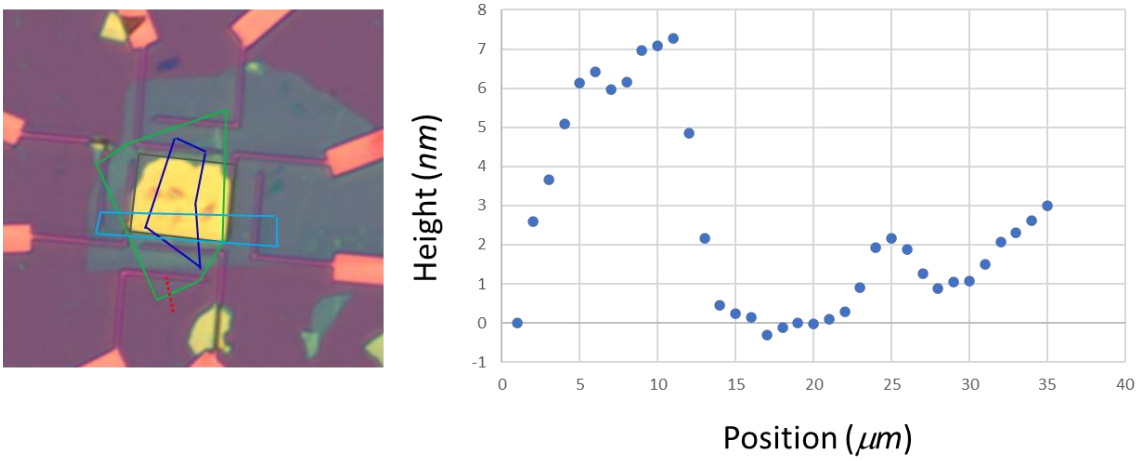

Figure 3.7 Atomic Force Microscopy on hBN. AFM data along the red dashed line on the optical image (left) is plotted as a function of position (Right). The data shows a jump of approximately 7nm at 12μm corresponding to the thickness and edge of the hBN respectively.

Device	Interlayer hBN Thickness
A	~ 10 nm
B	~7 nm
C	~ 8nm

Table 3.1 Interlayer hBN Thickness. The hBN thickness of the devices reported here.

3.5 Dry Transfer

A standard dry transfer technique [1] is used-along with a custom-built transfer microscope (Fig. 3.8)-to create the final graphene thermometer devices. A polymer stamp picks up the individual flakes and mechanically laminates them on top of the electrical contacts and other layers of the heterostructure. Then, a sequence of heating processes enables us to bring the materials into solid contact with the polymer to achieve lift off of the individual layers. The heterostructure is laminated directly onto a substrate with existing electrical contacts or a bare substrate with electrical contacts to be made afterwards.

The Transfer Microscope has three main components. At the bottom is a heated translation and rotation stage which controls the position, rotation and tilt of the target substrate. On top of this is an independently movable stamp stage which controls the lateral and vertical position of the polymer stamp relative to the target substrate. At the top is a confocal reflection microscope for visually aligning the materials. The bottom stage controls the heating and cooling process for initiating the lift off and drop off process for the graphene and hBN layers. The temperature is monitored by a thermocouple connected

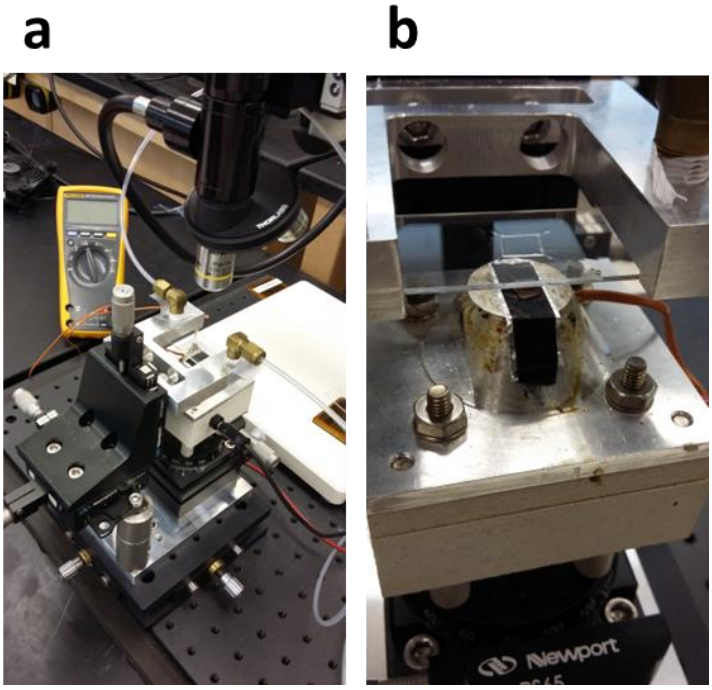

Figure 3.8 Dry Transfer Microscope. (a) A full image of the transfer microscope and (b) a close up on the heating stage and polymer stamp aligned over a substrate on the stage.

to the side of the heated aluminum chuck, to which the target substrate is mounted with double-sided carbon tape. The stamp stage has a fork arm which holds the polymer stamp. The fork has vacuum lines which allows the stamp to be held in place with a vacuum. The microscope at the top uses a lens tube design for a compact, low cost, yet effective system, which is mounted on a vertical rail system for focusing onto the target substrate.

To begin the dry transfer process, a polymer stamp is first created, which consists of 3 layers: glass, PDMS Gel, PPC. The base is a glass slide on which the stamp stage will be held. On top of the glass slide is a commercially available PDMS gel pad which is cut

into small squares (approximately 5mm x 5mm in size) and placed at the center of the glass slide. The PDMS acts as a soft platform for PPC such that the stamp can conform to the surface of the substrate. A 20% by weight solution of PPC in Anisole is prepared by dissolving PPC pellets in Anisole while stirring with a magnetic stirrer on a hotplate at 60℃ until the pellets are completely dissolved. The solution is then spin coated onto the PDMS at 4000 rpm for 40 s with ramp-up and ramp-down speeds of 1000 rpm/s. The Glass/PDMS/PPC stamp is then cured on a hotplate at 180℃ for 60 seconds. The Stamp is then loaded onto the fork on the transfer microscope by taping the sides of the glass slide and turning on the vacuum. The Stamp is aligned over the target substrate which has the flake to be picked up (Fig. 3.9).

We then align both the target substrate and stamp under the microscope and bring the two into contact. The stamp is lowered slowly using the micrometer stage. The portion of the stamp that is in contact with the substrate can be seen as the color changes. The relative angle of the target substrate is adjusted such that the stamp is in contact with the entire surface of the substrate at the same time. This method has shown the best results when picking up a flake. Once in contact, the stage is heated to 45℃, past the glass transition temperature of PPC (40℃). This promotes complete contact between the PPC and the flake. The stage is then allowed to cool back down to around 30℃ before the stamp is quickly lifted up, lifting off the flake.

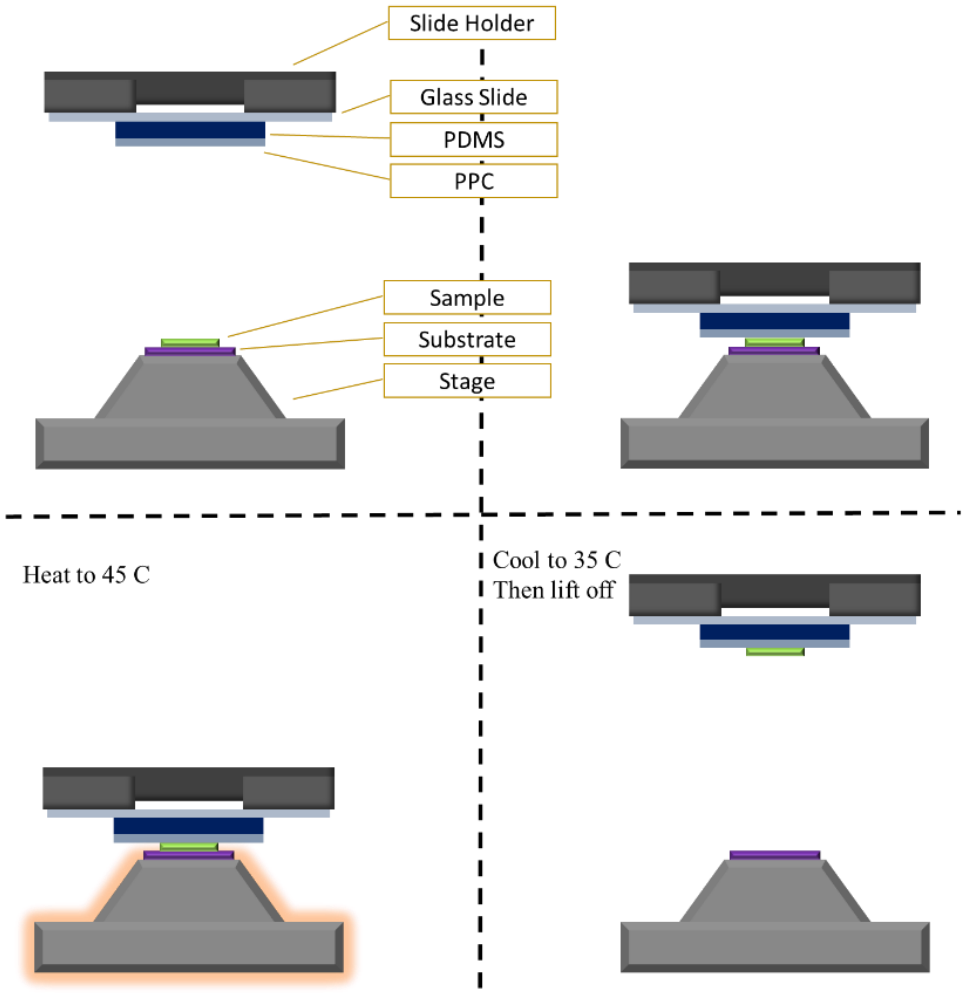

Figure 3.9 Dry Transfer Lift Off Process. Schematic of the transfer microscope and the steps to lift off a piece of material.

With a flake on the surface of the PPC, a new target substrate is loaded onto the transfer stage to either drop off the flake or to pick up a new flake to form a stack. In the case of picking up a new flake, the above procedure is repeated once the two flakes are aligned over each other. To drop off the fake, the stage is heated past the melting temperature of PPC (80℃) while the stamp is in contact with the substrate. This drops off

the flake and the PPC on the substrate. The PPC is then washed off by soaking in an acetone bath thus leaving behind the flake and cleaning off the PPC. This procedure of lift off and drop off is repeated to create the final heterostructure.

In an ideal heterostructure, the only layer that would contact any solvent or polymer is the very top layer; all subsequent layers are only in contact with the layers above and below. This keeps the interface between the layers as clean as possible; in our experience, this approach creates the best devices. This clean interface is achieved by lifting off each layer of the heterostructure in succession, using the previously picked up layer. Although this is ideal, it is not always practical as flakes may break during any lift-off step. Therefore, each device varies in quality due to varying number of layers that can be picked up in succession.

3.6 Fabrication of Electrical Contacts

For the final heterostructure, electrical contacts are created using electron beam lithography (EBL) (FIG. 3.10). In a conventional fabrication process, the heterostructure is first created and the electrical contacts are made to align to the desired layers of materials. For most of the devices studied here, the process is inverted: the electrical contacts are made with a predetermined pattern, and the materials are laid on top of the electrical contact. This minimizes the risk of exposing the materials to the electron beams and it also streamlines the alignment process (enabling the contacts to be at the exact position of the different material layers). To prepare a substrate for EBL, we first spin coat a layer of

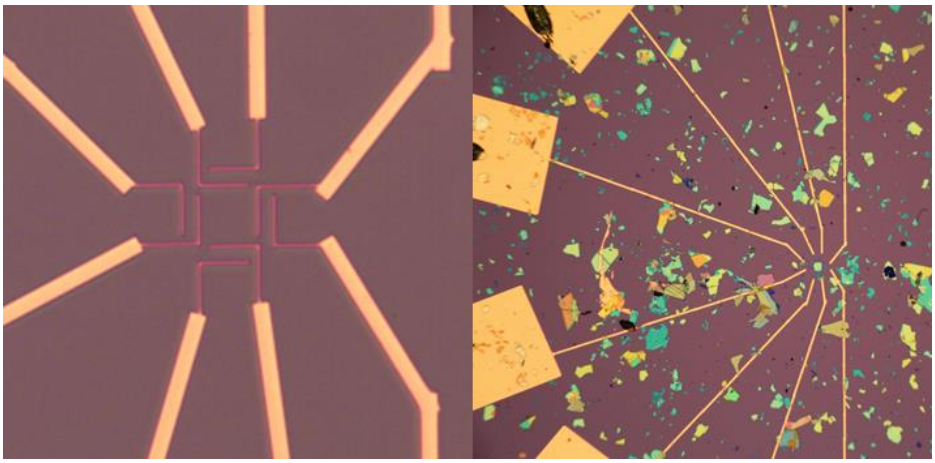

Figure 3.10 Prefabricated Electrical Contacts. Electrical contacts are created on a substrate on top of which individual flakes are transfered (Left). This process creates cleaner and higher-quality devices. Larger pads positioned in a crescent shape can be wire bonded to a larger sapphire substrate for measurements.

MMA copolymer onto the surface at 4000 rpm for 40 s with ramp-up and ramp-down speed of 1000 rpm/s. The layer is then cured at 180℃ for 10 minutes. A layer of PMMA EL 4 Electron Beam Resist is then spin coated and cured with the same specification. The pattern for the electrical contacts is then made using the Nanometer Pattern Generation System (NPGS) and loaded onto a Leo XB1540 focused ion beam milling system which has EBL capability. Once the substrate has been exposed to the electron beam the pattern is developed in a 1:3 MIBK:IPA solution. After this, 4nm of Titanium and 25 nm of gold are deposited onto the surface using an electron beam evaporator. The polymer resist is then removed by soaking in acetone, which leaves behind the desired pattern. The small ends of the contacts are arranged in a rectangle to be contacted with the individual graphene layers (FIG. 3.10). On the other end, the large contact pads are arranged in a half circle and are used to wire bond to a larger sapphire substrate to allow the device to be integrated into our measurement system.

3.7 Chip Carrier Fabrication and Device Integration

The devices are integrated into our measurement system via a home-built Chip Carrier (Fig. 3.11) that provides sufficient surface for electrical connections to measure current and apply voltages to our devices. We chose to use sapphire as the material for our chip carriers based on its thermal properties and insulating behavior. The sapphire provides good thermal contact to the silicon substrate for when we are cooling the device to cryogenic temperature for low-temperature measurements. It is also an insulator which allows us to form separate metal patterns on top to later be wire bonded to the small electrical contacts on the silicon substrate. These contacts electrically bridge our measurement system and the individual graphene layers in our graphene thermometer.

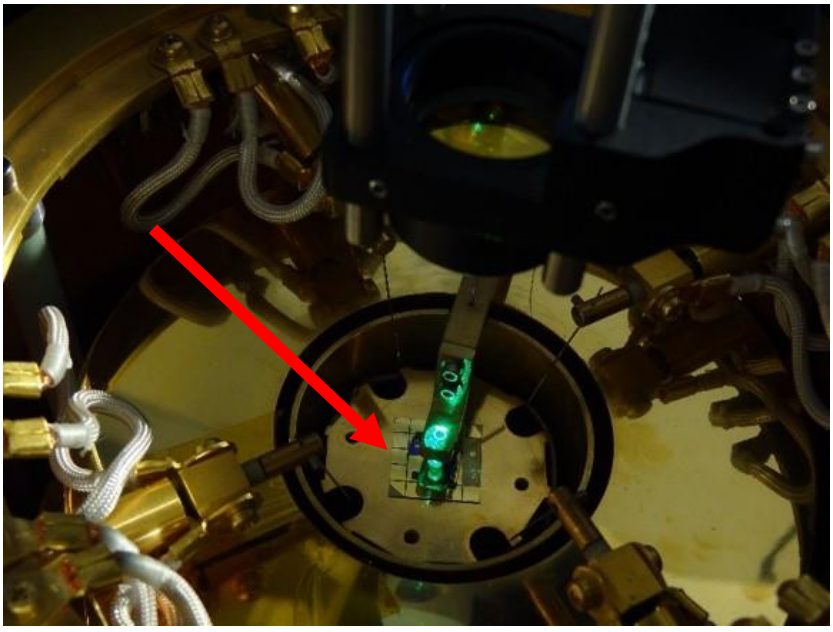

Figure 3.11 Device Integration via Chip Carrier. A device on the chip carrier sitting in the middle of an optical cryostat for measurement

The pattern for our chip carriers is fabricated using essentially the same photolithography procedure described above for the prepatterning of the silicon substrate. The only differences are in the photomask used, which carries the pattern shown in Fig. 3.12, and, instead of the etching step, a 4nm/200nm of Ti/Au was deposited using an electron beam evaporator.

Once the chip carrier is made, the device is attached on top and the proper electrical connections are made to the device via wire bonding. Using a diamond scribe, we first scratch away some of the SiO_2 on the bottom of the device's silicon substrate. This exposes the inner conductive silicon. The device is then secured on top of the large center gold area with a small amount of silver paint. This paint also forms an electrical connection between the center gold area and the silicon substrate; this connection can act as an electrical gate for the entire device. Then, the small electrical contacts on the device are wire bonded separately to the outer gold pads of the chip carrier. The probe needles in our measurement system will then be able to select which contact to apply voltage to and measure current from by contacting different parts of the chip carrier.

3.8 Device Comparison

As noted in this chapter's introduction. there are three main devices described here (Fig. 3.12). Device A consists of hBN/Graphene/hBN/Graphene/SiO_2, while Device B and Device C both consist of hBN/Graphene/hBN/Graphene/hBN. In Device A, the bottom layer of graphene is identified and the electrical contact is created on top of it. The top encapsulating hBN, the top graphene layer, and the middle hBN layer were picked up in

succession and laminated on top of the electrical contacts and the bottom layer of graphene. In Device B, the electrical contacts were first created. Then the bottom hBN layer was transferred to the center of the electrical contact. The middle hBN and bottom graphene were picked up in succession and laminated on top of the bottom hBN and put in contact with the vertical sets of electrical contacts. This is repeated for the top layer of hBN and graphene, but oriented to contact the horizontal set of electrical contacts. In Device C, the electrical contacts were first created. Then the bottom hBN layer was transferred to the center of the electrical contact. The remaining layers were picked up in succession and laminated simultaneously on top of the bottom layer of hBN and the electrical contacts.

The cleanliness of the devices is visibly different with best device being Device C with the least number of exposures to solvents and polymers. On the other hand, Device C also has the smallest overlapping area of the two graphene layers which forms the graphene thermometer. Device C has an overlap of approximately 30 μm^2. Device B has an overlap of approximately 50 μm^2. Device A has an overlap of approximately 150 μm^2. Although these devices have varying quality and size, they have similar photoresponse behavior which makes them viable graphene thermometers for this study.

Here in Chapter 3, we have described the methods for fabricating the devices we studied along with advances in techniques that improved the quality of our devices. In Chapter 4 we will describe the methods for measuring the photoresponse of these devices and determine if their behavior conforms to that of the graphene hot electron thermometer described in Chapter 2.

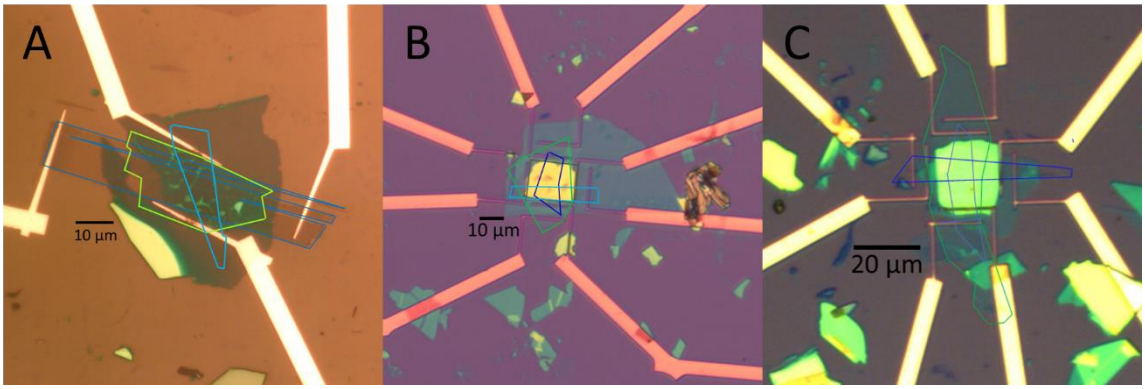

Figure 3.12 Device Comparison. Optical image of the 3 devices used in this study.

REFERENCES

[1] A. Castellanos-Gomez, M. Buscema, R. Molenaar, V. Singh, L. Janssen, H. S. J. van der Zant, G. A. Steele, Deterministic transfer of two-dimensional materials by all-dry viscoelastic stamping. *2D Mater. Lett.* **1**, 1-8 (2014).

[2] K. S. Novoselov, A. K. Geim, S. V. Morozov, D. Jiang, Y. Zhang, S. V. Dubonos, I. V. Grigorieva, A. A. Firsov, Electric field effect in atomically thin carbon films. *Science* **306**, 666-669 (2004)

[3] J.C.W.Song, N.M. Gabor, Electron quantum metamaterials in van der Waals heterostructures. *Nature Nanotech* **13,** 986–993 (2018).

[4] Y. Y. Wang, Z. H. Ni, et al., Raman Studies of Monolayer Graphene: The Substrate Effect, *J. Phys. Chem. C*, *112*, 10637–10640 (2008)

[5] Z. Ni, Y. Wang, T. Yu, and Z. Shen, Raman Spectroscopy and Imaging of Graphene, Nano Res 1: 273 291, (2008)

CHAPTER 4

Photoresponse of Graphene/hBN/Graphene Heterostructure

4.1 Introduction

We demonstrate the signatures of a functional graphene hot electron thermometer in the photoresponse of our Graphene/hBN/Graphene heterostructures (measurable out-of-plane photocurrent via heating of charge carriers). We characterize this photoresponse with a scanning photocurrent microscope integrated with a Multi-Parameter Dynamic Photoresponse Measurement[1] system. An ultra-fast pulsed laser is used to generate the electron-hole excited states. This laser is integrated with our electronics for operating the graphene thermometer by applying voltages and measuring the resulting current, thus mapping our photocurrent with several experimental parameters. This type of graphene-based heterostructure has been shown to provide an out-of-plane photocurrent and is expected to be non-linear with respect to incident laser power in the hot carrier regime[4]. This is due to the non-linear distribution of charge carriers in a Fermi Dirac Distribution. The non-linearity and characteristic response of the heterostructure will act as hall marks of a functional graphene thermometer. Below, we discuss the design of the optics for photoexcitation, the operating scheme of the device, and the behaviors of the resulting current.

4.2 Scanning Photocurrent Microscopy System

We generate hot electron-hole excited states in these devices using ultra short, infrared optical gating pulses (Fig 4.1). We utilize a MIRA 900 optical parametric oscillator tuned to the wavelength of 1200 nm to photoexcite our devices. This laser outputs femtosecond (150 fs) pulses at a repetition rate of 76 MHz. The output passes

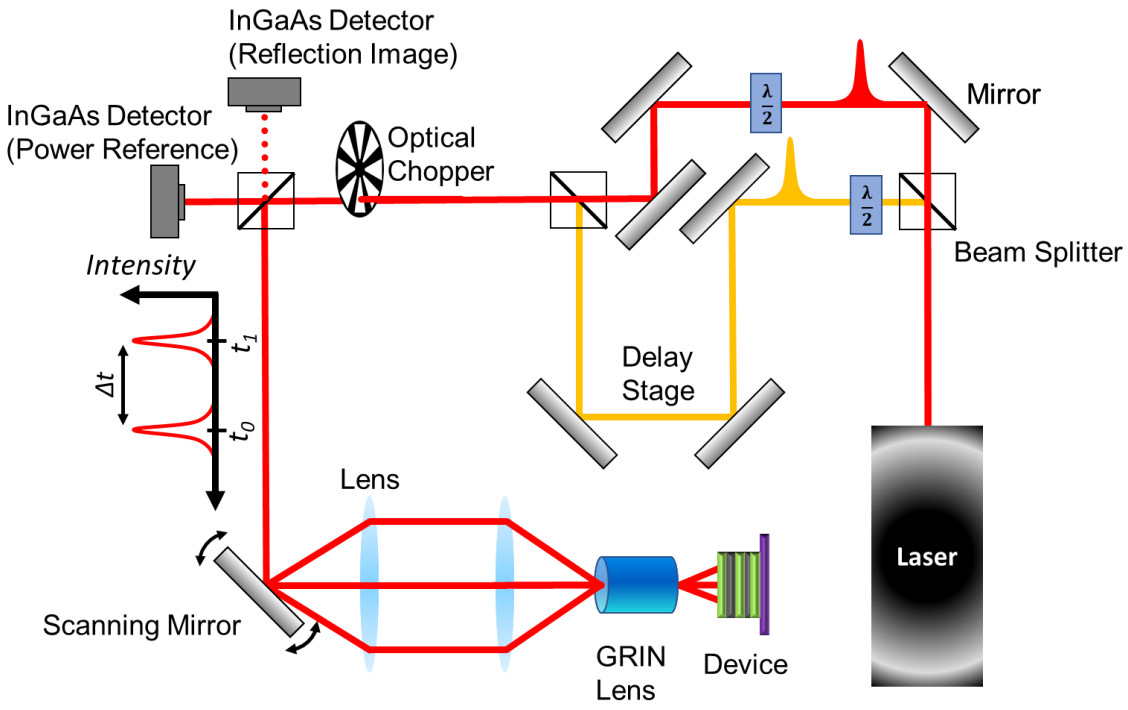

Figure 4.1 Scanning Photocurrent Microscopy. An ultrafast pulse laser is used to optically excite our devices. The laser pulses are optically delayed on a controlled delay stage, and the laser's focal position can be varied via a set of scanning optics.

through a 50/50 beam splitter which separates the beam into a reference path and a delay path. The delay path passes through a delay stage which varies the path length thus creating a time delay Δt between the pulses. The pulses are then recombined with another 50/50 beam splitter to reform a single beam. Both paths include a half waveplate such that the

two paths will be cross polarized to prevent interference of the pulses when recombined. The combined beam intersects an optical chopper that allows us to record the photoresponse using a Lock-In amplifier to measure the photoresponse with higher sensitivity and also remove any non-photoinduced responses. Finally, the beam arrives at a 90/10 beam splitter in which 10 % of the beam passes straight through the beam splitters and is collected with a InGaAs photodetector. The 10% of light collected at the InGaAs detector is used as a reference for the total power output of the laser. The 90% of the beam is reflected and redirected to a set of scanning optics for our microscopy measurement.

The scanning optics utilize a rotating galvo mirror and two lenses to control the light's angle of incidence onto the final objective, in this case a GRIN lens, thus changing the position which the laser focus on the device. In principle, the galvo mirror is set such that the center of rotation is at the focal point. The collimated beam, when incident upon the first lens, will then travel along a horizontal path but converge, with the point of convergence set at the focal length of the second lens. When the converging beam incident upon the second lens, the beam is once again collimated but now redirected to travel towards the focal point of the second lens. Thus, depending on the angle of the rotating mirror, we vary the angle of incidence of a collimated beam onto the back of our objective/Gradient Index of Refraction (GRIN) lens. This allows us to spatially scan the focal point of our laser.

The reflection image and photoresponse is then spatially correlated with the position of the laser's focal point to map the photoresponse of our devices. Any reflected light travels back along the same path as the incoming light, and a fraction passes straight

through the 90/10 beam splitter and is captured by a photodetector. The intensity of this reflections forms a reflection image of the device and allows us to calibrate the position of the laser's focal point with the angle of the galvo mirrors (Fig 4.2). The spatial resolution is limited by the laser's diffraction limit. In this case, the beam spot is approximately 1.5 μm in diameter. With this we can locate our device, spatially correlate the photoresponse, and photoexcite regions of interest on our devices as we operate our devices.

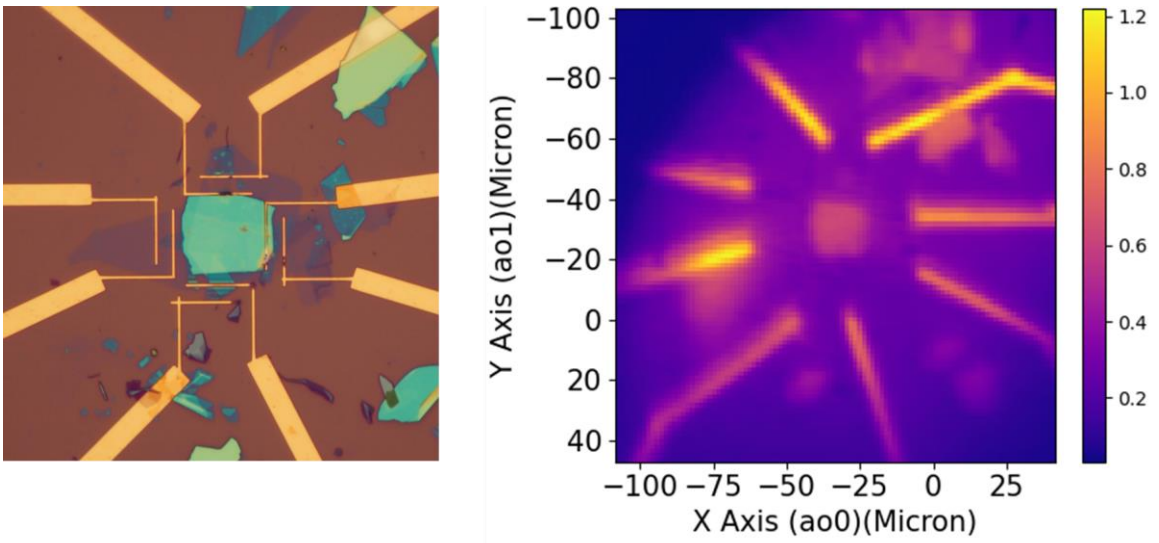

Figure 4.2 Reflection Imaging. Comparison of an optical image under a conventional microscope (left) and a reflection image generated from a scanning laser beam.

4.3 Graphene/hBN/Graphene Interlayer Photoresponse

We operate our devices by applying voltages to the graphene layers and measuring the generated photocurrent I_{PC}. As seen in the optical images of our devices (Fig. 3.12), the two layers of graphene form a cross with each other, and are connected to a pair of electrical contacts on opposite ends. To measure the transit of hot carriers across the hBN barrier in the out-of-plane direction, an interlayer voltage V_B is applied to the bottom layer G_B, while

probing the current in the top layer G_T (Fig. 4.3a). This is done with the two contacts on a layer bridged, thus creating essentially a single contact; Using this scheme we measure the purely interlayer photoresponse of these devices. Each optical pulse from our laser triggers a short burst of charge carriers that transit the hBN layer, which are then measured as an average interlayer photocurrent, I_{PC}. Photocurrent imaging shows a strong photoresponse only at the overlapping region of the two graphene layers; this is consistent with a purely interlayer photocurrent (Fig 4.3b). After the location of the device is identified, we can carefully study the response of our device by varying our two laser parameters: Excitation Power and Time Delay.

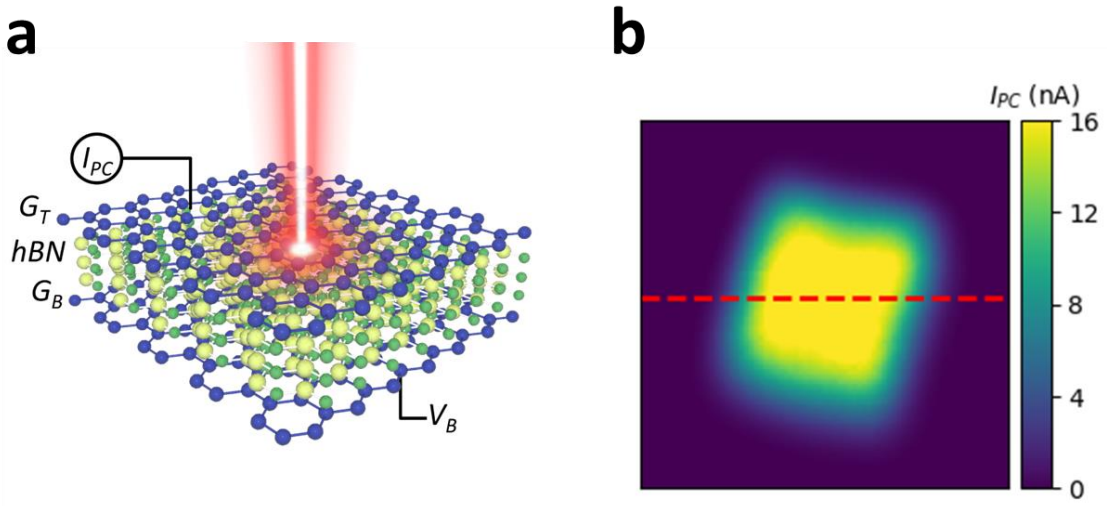

Figure 4.3 Interlayer Photocurrent Imaging. (a) Schematic of a Graphene-hBN-Graphene heterostructure device. The overlapping area is formed by crossing two long pieces of graphene. (b) Scanning photocurrent microscopy over Device C area shows a strong photocurrent where the two graphene layers overlap.

4.4 Hot Carrier Transport in a Graphene Thermometer

The average photoresponse of a Graphene/hBN/Graphene heterostructure is extracted and shown to exhibit behaviors consistent with the out-of-plane transport of hot carriers required for our graphene thermometer design. When measured along the dashed line in Fig 4.3b, and varying the laser power, we see that the photocurrent increases with laser power (Fig. 4.4a). We determine the average photoresponse by averaging over the active area of the device (between solid red lines in Fig. 4.5a). From a plot of I_{PC} vs. P (Fig. 4.5b), we see that this photocurrent increases super-linearly with P (blue line) and the data is well described by a power law fit (red line), where $I_{PC} \sim P^{\gamma}$ with $\gamma = 3.35$.

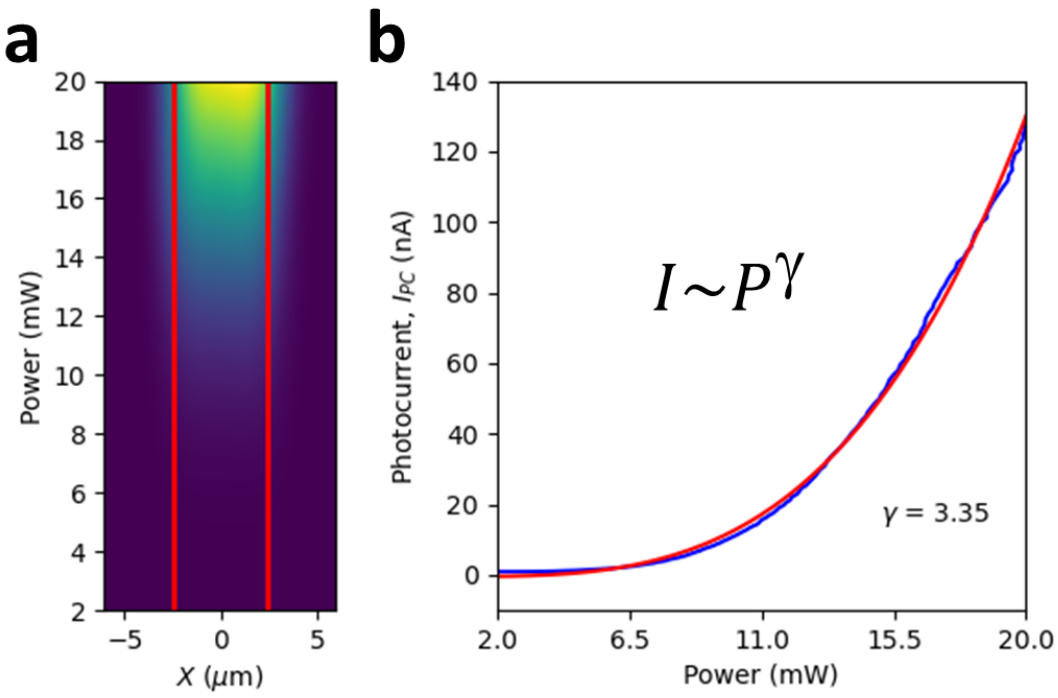

Figure 4.4 Power Dependent Interlayer Photocurrent. (a) Line scan across the dashed line in Fig. 4.3b as Laser power is increased. (b) Average photocurrent as a function of incident laser power (blue). A power law fit of $I \sim P^{\gamma}$ fits well to the data with $\gamma = 3.35$.

Strong super-linear photoresponse ($\gamma > 1$) gives rise to a short-lived, tenfold increase in the photocurrent when doubling the incident laser power. As shown in Fig. 4.5a. we resolve the dynamic, two-pulse photocurrent by separating identical laser pulses using the tunable time delay described in Section 4.2. When two gating pulses shine on the device simultaneously (time delay Δt = 0 ps), the resultant photocurrent is ten times greater than when the pulses are delayed by several picoseconds. As we increase Δt, I_{PC} decreases exponentially with a characteristic decay time τ = 1.31 ps (red dashed line, Fig. 4.5b)

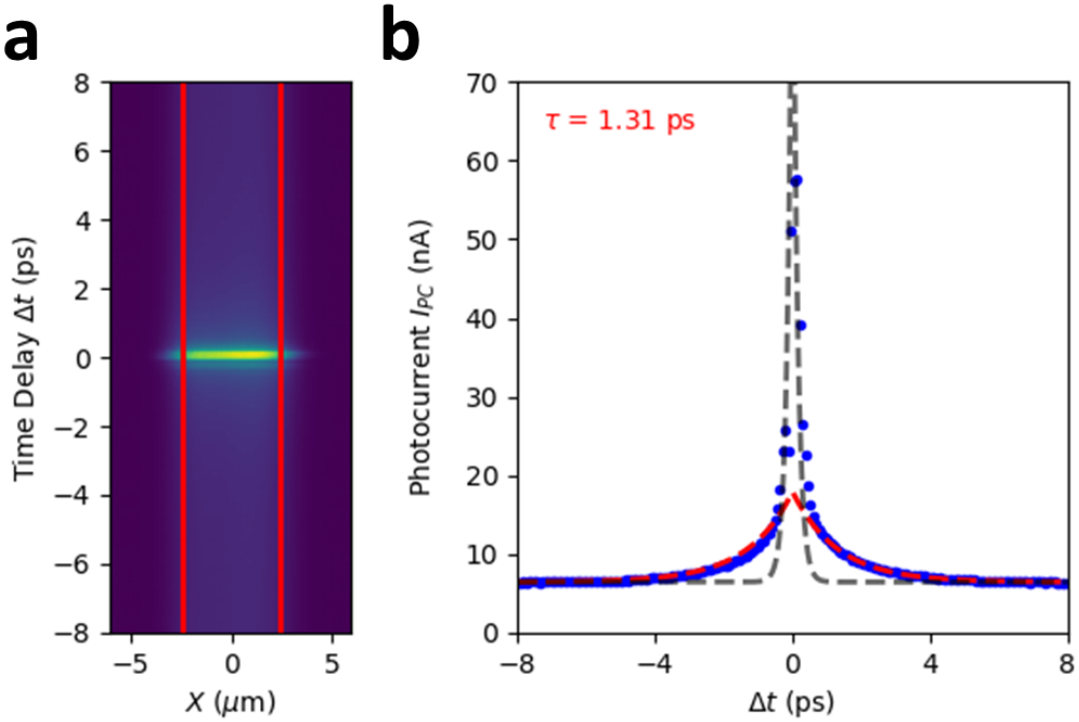

Figure 4.5 Graphene Heterostructure Response Time. (a) Line scan across the dashed line in Fig. 4.3b as pulse delay is varied. (b) Average photocurrent as a function of time delay. The photocurrent fits a double exponential decay with the slower decay time of 1.31 ps being the response time of the photocurrent. The fast decay is limited by our detection pulse duration but is consistent with an ultrafast relaxation of the photoexcited carriers via optical phonons.

The super-linear power dependence, tenfold increase in the two-pulse photocurrent indicates an important role played by the hot electron-hole excited state in the interlayer transport process and is consistent across all of our devices. Immediately after photoexcitation, the photon energy (E_{PH} = 1.03 eV) is divided between a photoexcited electron and hole (Fig. 4.6). Since the initial charge carrier kinetic energy ($K = E_{PH} / 2 \sim$ 0.515 eV) is significantly smaller than the hBN energetic barrier ($\Delta_h \sim 1.3$ eV for holes, $\Delta_e \sim 4.5$ eV for electrons[3]), direct transit is impossible. The population of excited electrons and holes is expected to then thermalize into a hot distribution, during which, fast Auger-

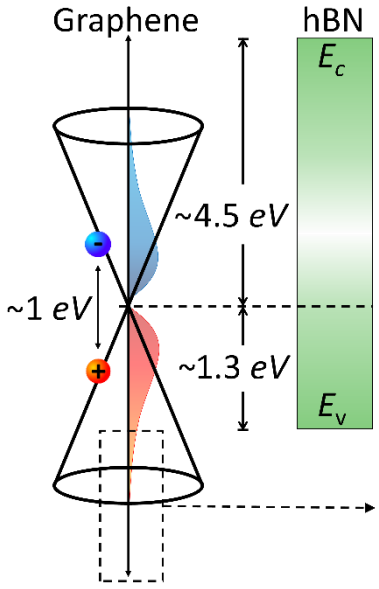

Figure 4.6 Thermionic Response of Photoexcited Graphene. The initial excitation with a ~1*eV* photon creates a population of electron and holes with insufficient energy to overcome the conduction (4.5 *eV*) or valence band (1.3 *eV*) of hBN. After thermalization, the exponential tail of the hot hole population dominates the photocurrent.

like scattering upconverts charge carriers[2] with sufficient energy to overcome the barrier. The exponentially decaying tail of this hot carrier distribution consists of hot carriers that can overcome the hBN barrier thus give rise to a super-linear dependence to excitation power.

The response time of these devices shows that we can extract carriers more quickly than the thermalized hot carriers cool. We are able to extract the effective temperature of the carriers even though the initial optical phonon cooling is still faster. That is, this interlayer transit of the hot carriers - mediated predominantly by holes, whose energy barrier $\Delta_h < \Delta_e$ - allows us to use the super-linear power dependence as an indicator for heating of charge carriers. This ensures that our graphene thermometer is functioning as intended as we vary our experimental parameters.

Here in Chapter 4, we have discussed the photoresponse of hot carriers in one of our graphene devices. We are able to extract a portion of the thermalized hot charge carriers before they cool in a time window of approximately 1.5 fs. The resulting photocurrent has a super-linear dependence with laser power which is consistent with the extraction of the high energy tail of a thermalized hot carrier distribution. This demonstrates a functioning graphene thermometer. In Chapter 5 we will calibrate this graphene thermometer by varying the interlayer voltage and extracting the effective electronic temperature.

REFERENCES

[1] T. B. Arp, N. M. Gabor, Multiple parameter dynamic photoresponse microscopy for data intensive optoelectronic measurements of van der Waals heterostructures, Review of Scientific Instruments **90**, 023702 (2019)

[2] I. Gierz, J. Petersen, M. Mitrano, et al. Snapshots of non-equilibrium Dirac carrier distributions in graphene. *Nature Mater* **12,** 1119–1124 (2013).

[3] N. Kharche & S. K. Nayak, Quasiparticle band gap engineering of graphene and graphene on hexagonal boron nitride substrate. Nano Lett. **11,** 5274_5278 (2011).

[4] Q. Ma, T. I. Andersen, et al., Tuning ultrafast electron thermalization pathways in a van der Waals heterostructure, Nature Physics **12**, 455-459 (2016)

CHAPTER 5

Thermionic Cascade of Dirac Carriers

5.1 Introduction

Graphene's unique carrier dynamics have garnered much attention in recent decades, especially due to potential technological applications that utilizing its unique infrared photoresponse and to study its novel electronic states that arise from the linear dispersion near its Dirac point. For example, it has shown promise as a broadband infrared absorber in technological applications[3,7,9], and demonstrated a uniquely efficient thermalization of photoexcited electrons into hot carrier populations[1,10,11]. Here we aim to utilizes this efficient generation of hot carriers in graphene to create a hot electron (thermionic) thermometer for studying the electron-hole excited states in graphene. As with any device, the tunability of its response has to be established to understand the underlying mechanisms that dictates its operation. Here we demonstrate a highly sensitive photoresponse which is consistent with a tunable electronic temperature that appears to peak at the Dirac point. This efficient heating leads to a thermionic cascade that enhances the photoresponse of this device. By extracting the electronic temperature, we also establish the operation and resolution of this graphene thermometer.

5.2 Tunable Interlayer Photoresponse in G-hBN-G Heterostructures

Under pulsed photoexcitation, the G-hBN-G photocurrent is extremely sensitive to the interlayer voltage. The photocurrent-voltage characteristics exhibit a sharp kink near V_B = 0 V (Fig. 5.1a). This behavior has not been observed in previous work and is not expected to occur via ordinary photo-thermionic emission nor by interlayer photon assisted-tunneling[8]. Comparing I_{PC} to the device resistance, we find that this sharp photocurrent increase coincides with the charge neutrality (Dirac) point of the top graphene layer (Fig. 5.1b). While I_{PC} remains super-linear with power at all voltages (Fig. 5.2), γ is also tuned via the interlayer voltage.

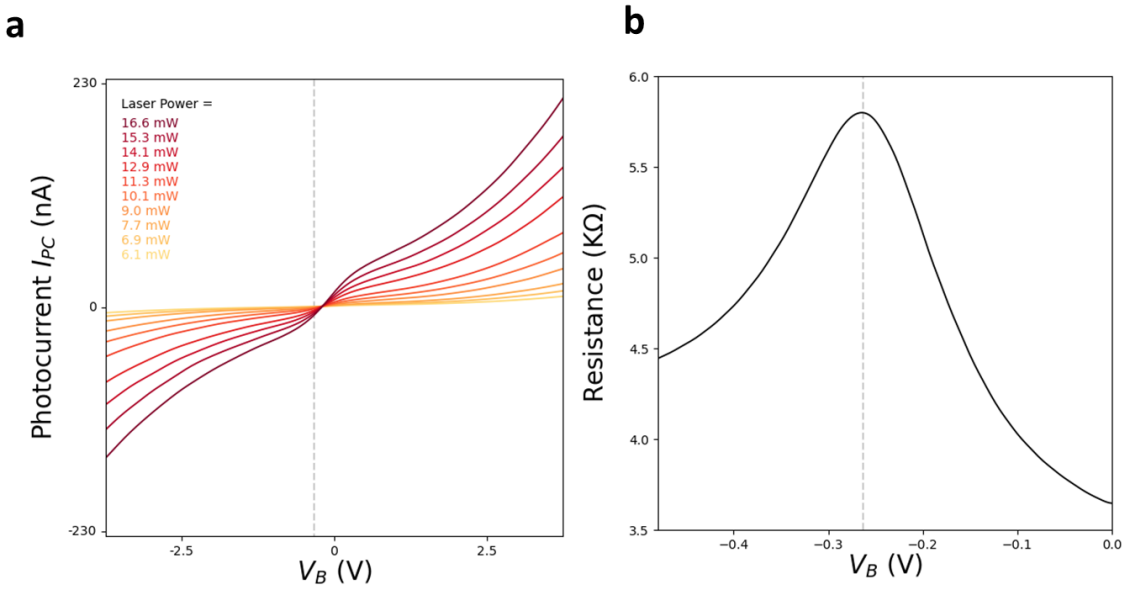

Figure 5.1 Photocurrent as a Function of Interlayer Voltage at Various Laser Power. (a) A plot of photocurrent as a function of interlayer voltage from Device A shows a kink near 0 V. This kink coincides with the location of the Dirac point as measured from the in-plane resistance shown in (b).

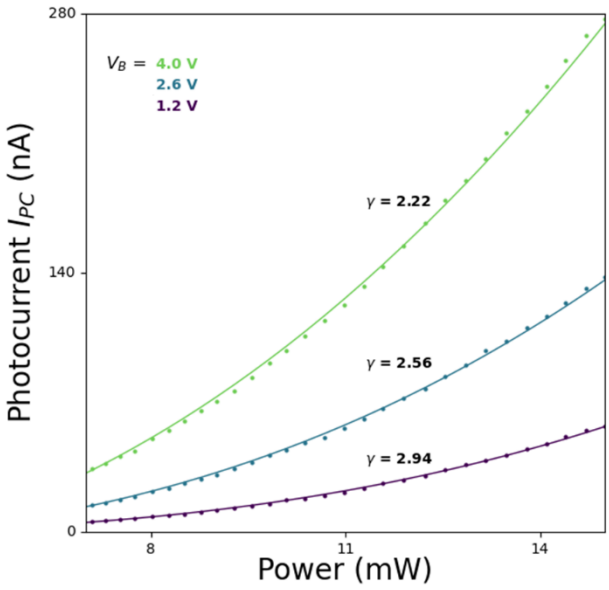

Figure 5.2 Photocurrent as a Function of Laser Power at Various Interlayer Voltages. The photocurrent remains super linear at different interlayer voltages (nonlinearity factor greater than 1).

While the interlayer photoconductance (dI_{PC}/dV_B) increases sharply near the Dirac point, the super-linear power dependence is strongly suppressed. Although γ increases gradually as we tune closer to V_D (Fig. 5.3), it also abruptly collapses in the same narrow voltage range over which the photoconductance is peaked. Proximity to the Dirac point also affects the characteristic time dynamics of the optically gated G-hBN-G photocurrent. This can be seen in Fig. 5.4, where the two-pulse inverse decay time $1/\tau$ is plotted vs. V_B. Importantly, the inverse decay time scales approximately linearly with the interlayer voltage.

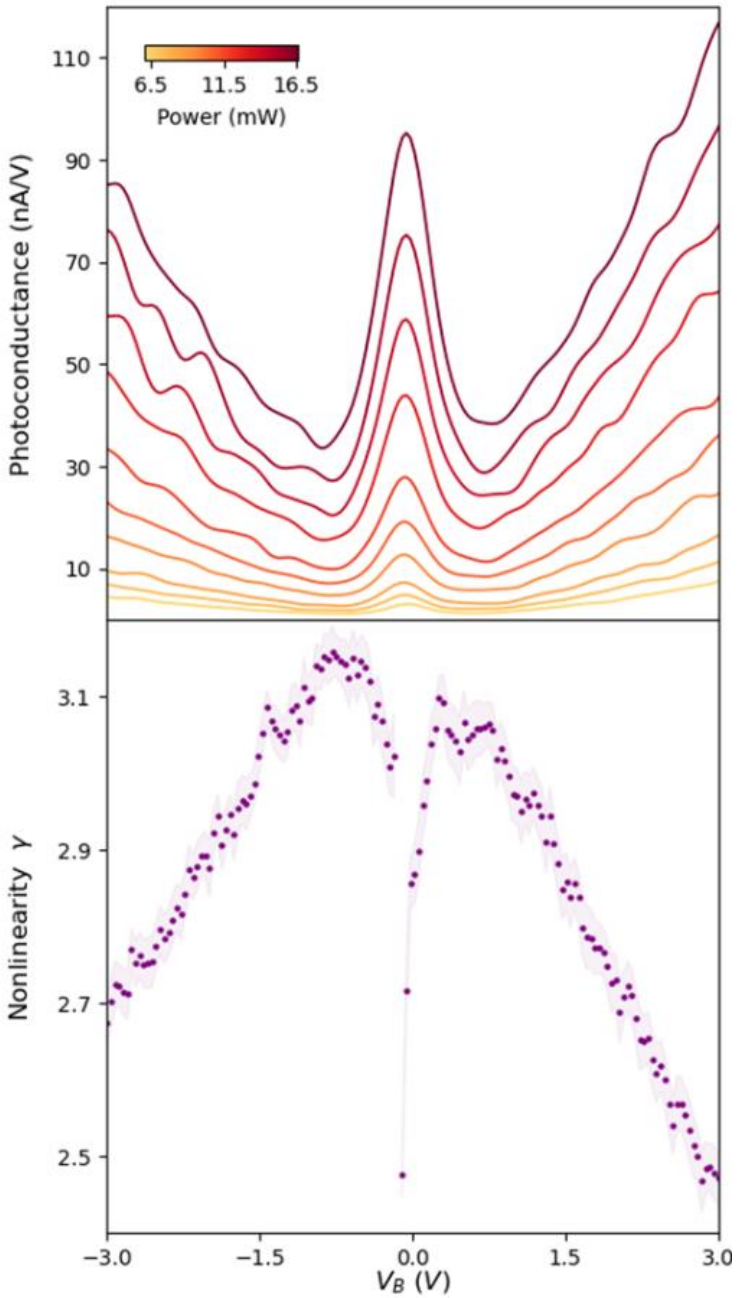

Figure 5.3 Interlayer Photoconductance and Nonlinearity. (top) The sharp kink in of the photocurrent shows up as a photoconductance peak. Over the voltage range which the peak appears the Nonlinearity is suppressed, however remains super linear across the full voltage range suggesting the persistence of hot carrier transport over the entire operating range.

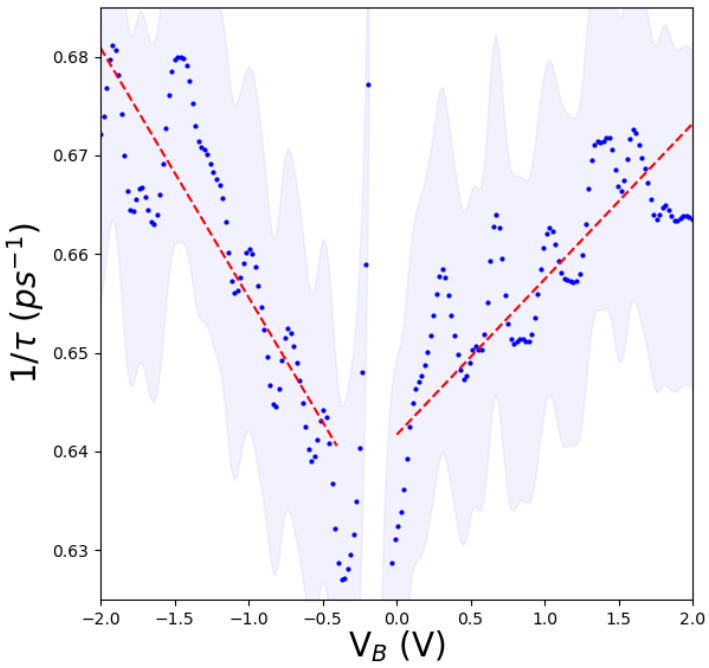

Figure 5.4 Hot Carrier Transit Time. The transit of hot carrier is longest when the voltage is small and has a seemingly linear response to the interlayer voltage. This suggests that the drift of hot carriers across the hBN contributes to our photocurrent.

5.3 Signature of Thermionic Cascade in Graphene

The salient sensitivity of the photocurrent to the interlayer voltage suggests that a voltage-tunable electronic temperature drives the interlayer transport on top of the voltage driven-drift of the carriers. The enhanced interlayer photoconductance and suppressed super-linearity suggests that the heating of the electron-hole population becomes highly efficient when the device is tuned to the Dirac point. This efficient heating gives rise to a thermionic cascade in which a large population of ultra-hot carriers is available to cascade through the hBN.

The transit of hot carriers sets the voltage dependence of the ultrafast response time τ (Fig 5.4). Cascading carriers are driven by the interlayer electric field $\vec{\mathscr{E}}$ and accelerate through the interface. As $\vec{\mathscr{E}}$ increases, charge carriers transit more quickly. Carriers must travel a distance L with an electric-field dependent drift velocity $v = \mu\varepsilon$ where μ is the charge carrier mobility. From the velocity, we get an expression for the transit time $\tau = L/\mu\varepsilon = L^2/\mu V_B$, where $\mathscr{E} = V_B/L$ is controlled by the interlayer voltage V_B. Combining the hBN thickness L = 10 nm for Device 1 with the slope from Fig. 2f, we estimate the mobility: $\mu = |s|L^2 = (40\text{ V ps})^{-1}(10\ nm)^2 \approx 2.5*10^{-2}$ cm^2/V*S, consistent with the very low out-of-plane hole mobility of hBN[2].

To demonstrate the efficient heating of the carriers and nature of this thermionic cascade, we extract the electronic temperature as a function of interlayer voltage. Since the photocurrent is superliner with respect to incident laser power across the entire interlayer voltage range, the hot carrier transport picture of the photocurrent remains valid. Thus, we can model the photocurrent as a function of interlayer voltage - which varies the chemical potential - and the electronic temperature (Fig. 5.5a).

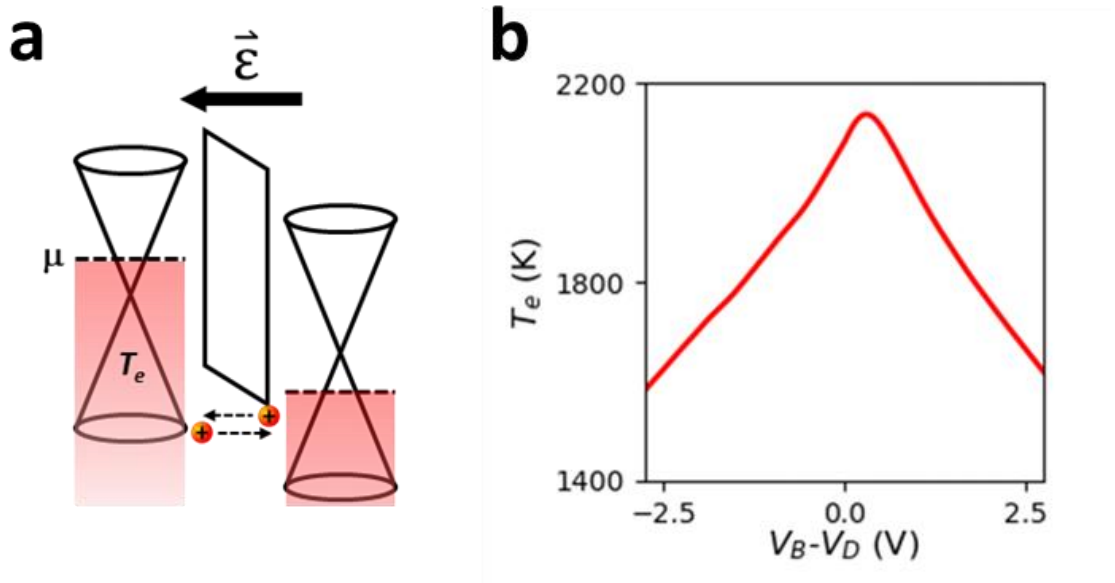

Figure 5.5 Model and Extracted Electronic Temperature. (a) A schematic of the graphene thermometer in which the total photocurrent is the sum of the counter propagating carriers when an interlayer voltage is applied. (b) The extracted electronic temperature from the 16.6 mW photocurrent curve is shown in Figure 5.1.

5.4 Calibrating the Graphene Thermometer

We extract the electronic temperature at each voltage that reproduces the photocurrent-voltage profile of our data in order to calibrate our graphene thermometer. The details of the modeling of this electronic temperature are discussed in Chapter 6. The result shows an electronic temperature that peaks near the Dirac point as a function of interlayer voltage (Fig. 5.5b). This electronic temperature exceeds 2000 K, which is consistent with other studies involving photoexcited graphene[1,5,6,12].

This electronic temperature profile suggests that this device geometry acts as a highly sensitive hot electron temperature probe at the Dirac point. We can determine the

sensitivity of this probe by considering the relationship between the photocurrent and electronic temperature. The electronic temperature, T_e, is expected to be proportional to the excitation power in which $T_e \sim P^{1/2}$ [4]. Having determined earlier that $I_{PC} \sim P^3$ where P is the excitation power and the exponent is the nonlinearity factor of the photocurrent, we can determine that $T_e \sim I_{PC}^{1/6}$. The measurable resolution of our electronic temperature $\Delta T_e = \Delta I_{PC}*(dT_e/dI_{PC}) = \Delta I_{PC}*(1/6)*(I_{PC})^{(-5/6)}$ where ΔI_{PC} is the resolution of our photocurrent measurement. Given that our measurement resolution is on the order of 10^{-9} A, and the typical photocurrent near the Dirac point is approximately 10^{-9} A, this $\Delta T_e \sim 1$ mK and a sensitivity $\Delta T_e/T_e \sim 5*10^{-7}$.

Here in Chapter 5, we observed the photocurrent's response to interlayer voltage and extracted the electronic temperature from this photocurrent. The photocurrent is highly sensitive near the Dirac point and is consistent with a tunable electronic temperature that peaks at the Dirac point. In Chapter 6 we will describe the details for modeling this electronic temperature, which has enabled us to extract its profile.

REFERENCES

[1] D. Brida, A. Tomadin, et al., Ultrafast collinear scattering and carrier multiplication in graphene. *Nature Commun.* **4**, 1987 (2013).

[2] R. Dahal et al., Anisotropic charge carrier transport in free-standing hexagonal boron nitride thin films, Appl. *Phys. Express* **9** 065801 (2016)

[3] D.K. Efetov, RJ. Shiue , Y. Gao, *et al.* Fast thermal relaxation in cavity-coupled graphene bolometers with a Johnson noise read-out. *Nature Nanotech* **13,** 797–801 (2018).

[4] C. Ferrante, A. Virga, L. Benfatto, M. Martinati, D. De Fazio, U. Sassi, C. Fasolato, A. K. Ott, P. Postorino, D. Yoon, G. Cerullo, F. Mauri, A. C. Ferrari, T. Scopigno. Raman spectroscopy of graphene under ultrafast laser excitation. *Nat. Commun.* **9**, 308 (2018)

[5] I. Gierz , J. Petersen, M. Mitrano, et al. Snapshots of non-equilibrium Dirac carrier distributions in graphene. *Nature Mater* **12,** 1119–1124 (2013).

[6] J. C. Johannsen et al. Direct View of Hot Carrier Dynamics in Graphene. *Phys. Rev. Lett.* **111**, 027403 (2013).

[7] S. Kim, M. S. Jang, et al., Electronically Tunable Perfect Absorption in Graphene, *Nano Lett.*, 18, 2, 971–979, (2018)

[8] A. Kuzmina, M. Parzefall, et al., Resonant Light emission from Graphene/Hexagonal Boron Nitride/Graphene Tunnel Junctions, *Nano Lett.*, 21, 19, 8332-8339, (2021)

[9] M. Long., E. Liu, et. al., Broadband Photovoltaic Detectors Bawsed on an Atomically Thin Heterostructure, *Nano Lett.*, 16, 4, 2254–2259 (2016)

[10] J. C Song, K. J. Tielrooij, F. H. Koppens, & L. S.Levitov, Photoexcited carrier dynamics and impact-excitation cascade in graphene. *Phys. Rev. B* **87**, 155429 (2013).

[11] K. J. Tielrooij, et al. Photoexcitation cascade and multiple hot-carrier generation in graphene. *Nature Phys.* **9**, 248–252 (2013).

[12] A. Tomadin, D. Brida, G. Cerullo, A. C. Ferrari, M. Polini. Nonequilibrium dynamics of photoexcited electrons in graphene: Collinear scattering, Auger processes, and the impact of screening. *Phys. Rev. B* **88**, 035430 (2013)

CHAPTER 6

Modeling Photocurrent and Extracting Electronic Temperature

6.1 Introduction

We estimate the electronic temperature based on our phenomenological photocurrent model, and show how we are able to tune the heating and cooling efficiency of the electron-hole excited states. This is achieved by first modeling the photocurrent in the hot carrier regime in which thermionic cascade dominates. Then we can determine the electronic temperature required to match our photocurrent data. However, a generalized modeling of the photocurrent in a G-hBN-G device is difficult due to inherent asymmetries in the system (unequal initial doping)[2]. Below, we present a generalized calculation to show that the initial doping of our devices is small. This enables us to approximate the electronic temperature with the assumption that the devices' electrostatics are fully symmetric. This approximate electronic temperature has excellent agreement with the profile of expected (calculated) electronic temperature based on the electronic heat capacity of graphene.

6.2 Generalized Chemical Potential Calculation

We determine the initial doping by considering the capacitive coupling between layers in our G-hBN-G heterostructure and by adapting a similar approach as reference [2]. As we apply an interlayer voltage to G_B, the quantum capacitance of graphene describes the change in the charge density (thus chemical potential), while the geometric capacitance

describes the potential drop across the two graphene layers. The interlayer voltage is the sum of the change in chemical potentials and the potential drop across the layers.

A general relationship can be written with each graphene layers having an initial doping (Eq 6.1), where e is the electron charge, V_B is the interlayer voltage, μ_T is the chemical potential of the top layer of graphene, μ_{T0} is the initial doping (chemical potential) of the top layer of graphene, μ_B is the chemical potential of the bottom layer of graphene, μ_{B0} is the initial doping of the bottom layer of graphene, E is the electric field between the two graphene layers, and d is the separation between the graphene layers (in other words, the interlayer hBN thickness).

$$eV_B = \mu_T - \mu_{T0} + \mu_{B0} - \mu_B + eEd \tag{6.1}$$

$$V_B = \mu_T - \mu_{T0} + \mu_{B0} - \mu_B + Ed \quad ; in\ units\ of\ eV \tag{6.2}$$

We can relate the chemical potentials and the electric field by the change in charge density such that we end up with a relationship between V_B and either μ_T or μ_B. To do this we must first determine the relationship between μ_T and μ_B.

When an interlayer voltage is applied, the change in charge density in one layer is equal and opposite that of the other layer (Eq. 6.3). Given the density of states of graphene, we can express the chemical potential in terms of the change in charge density (Eq. 6.4). By combining equation 6.3 and 6.5 we can express the relationship between μ_T and μ_B (Eq. 6.5). We can then express μ_T as a function of μ_B and vice versa (Eq 6.6.1 and Eq 6.6.2). The electric field, E, between the layers can also be expressed in terms of the chemical

potential if we consider the two graphene layers as a capacitor with a dielectric, hBN. We can now rewrite Eq. 6.2 in terms of either μ_T or μ_B, Eq. 6.7.1 and Eq. 6.7.2 respectively. Although there is still the sign of the opposing layer to consider in these two expressions, they are entirely determined by whether or not the quantity under the square root is positive, which only depends on the layer in question. We then can solve for the combination of μ_{T0} and μ_{B0} which simultaneously satisfies both the top layer and bottom layer Dirac point voltage, $V_B(\mu_T = 0)$, $V_B(\mu_T = 0)$, which yields the initial doping of both layers.

$$\Delta n_T = -\Delta n_B \tag{6.3}$$

$$\mu_i = -\frac{\hbar v_F}{e}\sqrt{\pi|n_0 + \Delta n_i|}\,sign(n_0 + \Delta n_i) \tag{6.4.1}$$

$$sign(\mu_i)\mu_i^{\,2} = -\frac{\hbar^2 {v_F}^2}{e^2}\pi(n_0 + \Delta n_i) \tag{6.4.2}$$

$$sign(\mu_i)\mu_i^{\,2} = sign(\mu_{i0})\mu_{i0}^{\,2} - \frac{\hbar^2 {v_F}^2}{e^2}\pi(\Delta n_i) \tag{6.4.3}$$

$$sign(\mu_T)\mu_T^{\,2} - sign(\mu_{T0})\mu_{T0}^{\,2} = -sign(\mu_B)\mu_B^{\,2} + sign(\mu_{B0})\mu_{B0}^{\,2} \tag{6.5}$$

$$\mu_T = sign(\mu_T)\{sign(\mu_T)[-sign(\mu_B)\mu_B^{\,2} + sign(\mu_{T0})\mu_{T0}^{\,2} + sign(\mu_{B0})\mu_{B0}^{\,2}]^{1/2}\} \tag{6.6.1}$$

$$\mu_B = sign(\mu_B)\{sign(\mu_B)[-sign(\mu_T)\mu_T^{\,2} + sign(\mu_{T0})\mu_{T0}^{\,2} + sign(\mu_{B0})\mu_{B0}^{\,2}]^{1/2}\} \tag{6.6.2}$$

$$V_B(\mu_T) = \mu_T - \mu_{T0} + \mu_{B0} - sign(\mu_B)\{sign(\mu_B)[-sign(\mu_T)\mu_T{}^2 + sign(\mu_{T0})\mu_{T0}{}^2 + sign(\mu_{B0})\mu_{B0}{}^2]\}^{1/2} - \frac{de^3}{\pi\hbar^2 v_F{}^2}[sign(\mu_T)\mu_T{}^2 - sign(\mu_{T0})\mu_{T0}{}^2] \quad (6.7.1)$$

$$V_B(\mu_B) = -\mu_B - \mu_{T0} + \mu_{B0} + sign(\mu_T)\{sign(\mu_T)[-sign(\mu_B)\mu_B{}^2 + sign(\mu_{T0})\mu_{T0}{}^2 + sign(\mu_{B0})\mu_{B0}{}^2]\}^{1/2} + \frac{de^3}{\pi\hbar^2 v_F{}^2}[-sign(\mu_B)\mu_B{}^2 + sign(\mu_{B0})\mu_{B0}{}^2] \quad (6.7.2)$$

When calculating the initial doping, we first determine the Dirac point voltage, V_D, for each layer of graphene. This is the interlayer voltage at which a layer of graphene in a device reaches the Dirac point ($\mu = 0$). This is done by measuring the in-plane resistance across one of the graphene layers by applying a source voltage to one of the contacts and measuring the dark current on the opposing contact while using the other layer as a gate. The resistance peak shows the Dirac Point voltage, $V_B(\mu_i = 0) = V_{D,i}$, for each layer of graphene (Fig 6.1). All of our devices show a resistance peak close to 0 V of interlayer

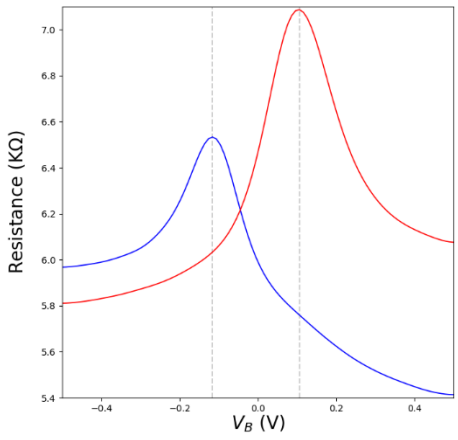

Figure 6.1 Dirac Point Voltage Extraction. The Voltage at which a layer of graphene is at the Dirac point is extracted from the dark in-plane resistance as a function of interlayer voltage, with the opposing layer acting as a gate.

voltage which suggests they are close to being charge neutral. This can be confirmed in the following calculation for the initial doping in terms of the starting chemical potential.

Using equation 6.7.1 and 6.7.2, we first select an arbitrary μ_{T0} and solve for $V_{D,T}$ and $V_{D,B}$ over a series of test μ_{B0} values. By interpolating μ_{B0} as a function of $V_D$we can determine the value of μ_{B0} with the chosen μ_{T0} which yields the correct Dirac point voltage for both equations. This is repeated over a series of μ_{T0}. The result are two sets of μ_{T0} and μ_{B0} in which one set satisfies $V_{D,T}$ and the other satisfies $V_{D,B}$. By plotting μ_{T0} as a function of μ_{B0} the intersection between the two curves is the single combination of μ_{T0} and μ_{B0} which satisfies both $V_{D,T}$ and $V_{D,B}$ simultaneously. We confirm an accurate μ_{T0} and μ_{B0} were found by solving for $V_{D,T}$ and $V_{D,B}$ with the calculated values and ensure the difference between the calculated and experimental $V_{D,T}$ and $V_{D,B}$ are at least three orders

Device	μ_T (eV)	$\mu_B(eV)$
A	0.173	0.173
B	-0.096	-0.053
C	0.071	0.067

Table 6.1 Initial Doping. Calculated initial doping for all three devices presented in this study. The initial doping is relatively small compared to the Dirac Cone which is considered to be valid up to approximately 1.5eV such that we may assume a simpler purely symmetric model for the photocurrent.

of magnitude smaller than the actual Dirac point voltages. Table 6.1 shows the calculated initial doping. Device B and Device C are calculated using the Dirac point voltage obtained from the minimum dark current transconductance of both layers of graphene. For Device A, the bottom layer only has one working contact, therefore no dark current was measured

for the bottom layer and we assume the Dirac point voltage is the same as the top layer. This is a reasonable assumption since both layers a given device are made in a similar time frame and stored under the same conditions which yields similar doping as seen in Device B and Device C.

6.2 Photocurrent Model

The photocurrent depends on the chemical potential and the electronic temperature at a specific interlayer voltage (Fig. 6.2). The total photocurrent I_{PC} is the sum of the counter propagating photocurrent originating from each layer of graphene $I_{PC} = I_B - I_T$ where I_B and I_T are the current from the bottom and top layer respectively. The magnitude of the photocurrent from each layer depends on the population of carriers with high enough energy to overcome the hBN barrier. We calculate this by integrating all carriers with energy larger than the barrier, U_0. Since the photocurrent is expected to be dominated by the transport of holes, we shall integrate the population of holes up to the valence band energy, $U_0 = 1.3\text{eV}$[1], from negative infinity (Eq 6.8.1).

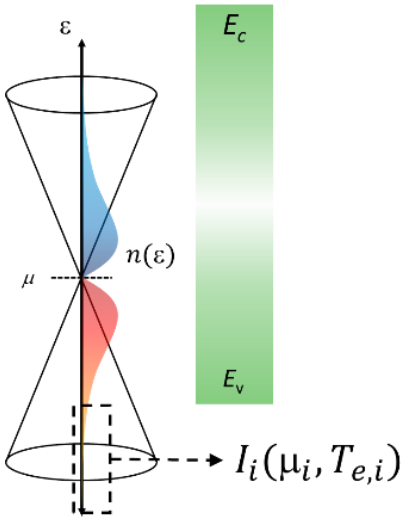

Figure 6.2 Photocurrent Parameters. The population of carriers above the barrier depends on the shape of the final thermalized distribution which depends on the position of the chemical potential at the time of photoexcitation and the electronic temperature after thermalization.

$$I_i = e \int_{-\infty}^{-U_0} \rho(\varepsilon) f(-\varepsilon + \mu_i)\, d\varepsilon \tag{6.8.1}$$

$$I_i = C \int_{-\infty}^{0} |\varepsilon - U_0| f(-\varepsilon + U_0 + \mu_i)\, d\varepsilon \tag{6.8.2}$$

Here, e is the electron charge, $\rho(\varepsilon)$ is the density of states of graphene as a function of energy, f is the Fermi Dirac Distribution, and μ_i is the respective chemical potential for the ith layer. We can perform a change of variable to change the integration limit from -U_0 to 0 such that the integral has known analytic solutions (Eq. 6.8.2). The full integral is expressed in Equation 6.8.3. Here, C captures all of the constants from the density of states and the electron charge ($2e/\pi\hbar^2 {v_F}^2$), k_B is the Boltzmann Constant, and T_e is the

electronic temperature. Solving both integrals we get Equation 6.8.4, where Li is a polylogarithmic function. In Equation 6.8.4, we see that are the electronic temperature and the chemical potential. We can now rewrite the total photocurrent in terms the two parameters in Equation 6.8.4, $T_{e,i}$ and μ_i(Equation 6.9). Since the chemical potential can be determined at any interlayer voltage value, as seen in section 6.2, this photocurrent model allows us to extract the electronic temperature from our photocurrent data.

$$I_i = C \int_{-\infty}^{0} \frac{-\varepsilon}{e^{\beta(U_0+\mu_i)}e^{-\beta\varepsilon}} + \frac{U_0}{e^{\beta(U_0+\mu_i)}e^{-\beta\varepsilon}}\, d\varepsilon \quad ; \beta = \frac{1}{k_B T_{e,i}} \tag{6.8.3}$$

$$I_i = C\left[\frac{1}{\beta^2} Li_2\left(e^{-\beta(U_0+\mu_i)}\right) + \frac{1}{\beta} ln\left(e^{-\beta(U_0+\mu_i)} + 1\right)\right] \tag{6.8.4}$$

6.3 Extraction of Electronic Temperature

The electronic Temperature and its profile are extracted by determining the temperature required to match our photocurrent data across the interlayer voltage values in our experiment. However, we have one equation for the photocurrent which has four unknowns, two separate chemical potentials and two separate electronic temperatures. Since the initial doping of our devices are relatively small, we will resolve this by considering the purely symmetric case in which the chemical potentials start off at 0 eV for both layers. In this case, as the interlayer voltage is varied, μ_B and μ_T change in opposite directions but remains equal in magnitude. This allows us to generalize to a single chemical potential and electronic temperature to represent both layers. Since the electronic temperature is the result of the charge carriers retaining the energy from photoexcitation,

the final temperature would depend on the electronic heat capacity of graphene. This electronic heat capacity depends purely on the position of the chemical potential which is symmetric with respect to interlayer voltage in this scenario (Section 6.4).

Since the chemical potential can be directly determined from the interlayer voltage, as seen in Eq. 6.7.1 and Eq. 6.7.2, we can simplify equation 6.9 further as a function of the interlayer voltage (Eq. 6.10)

$$I_{PC} = I_B(\mu_B T_{e,B}) - I_T(\mu_T T_{e,T}) \tag{6.9}$$

$$I_{PC}(V_B) = I_B(\mu(V_B), T_e(V_B)) - I_T(-\mu(V_B), T_e(V_B)) \tag{6.10}$$

With the photocurrent measured and the chemical potential determined by electrostatics, the electronic temperature can now be solved for numerically. At each interlayer voltage value, the chemical potential is first calculated, and a series of test values for T_e is used to calculate a series of possible I_{PC}. By interpolating the test I_{PC} as a function of test T_e, we can then solve for the T_e which yields the measured photocurrent. Due to the inherent asymmetry of the photocurrent, we must make an approximation of the Dirac point location while maintaining the profile of the photocurrent. We first center the data to the Dirac point of the layer from which we are measuring the photocurrent, such that $V_B = 0\ V$ in our model corresponds to the Dirac point of the top layer of graphene. The photocurrent is then offset so that it is zero at $V_B = 0\ V$. This process maintains the profile of the photocurrent and only makes an approximation of the Dirac point voltage in the data. From this basis we can extract the electronic temperature.

6.4 Modeling Electronic Temperature by Heat Capacity

We model the expected electronic temperature profile of graphene based purely on the electronic heat capacity of graphene as a comparison to the extracted electronic temperature profile. By calculating the difference in total energy stored by charge carriers at two different temperatures, T_0 and T_1, at a specific chemical potential, μ, the amount of energy stored by the electronic heat capacity is determined (Fig 6.3). This in turn enables us to determine the final temperature of the thermalized hot carriers to store a fixed amount of energy at a specific chemical potential.

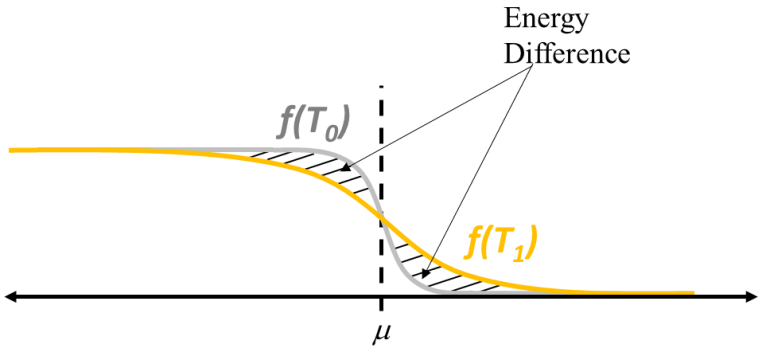

Figure 6.3 Electronic Heat Capacity. The Energy stored is the energy difference between two Fermi Dirac Distributions at different temperatures.

We start by formulating the general expression for the energy stored per unit area of graphene. The energy difference between two population of carriers at two different electronic temperatures is expressed in equation 6.11,

$$dE = \int_{-\infty}^{\infty} \rho(\varepsilon)[f(\varepsilon-\mu,T_1) - f(\varepsilon-\mu,T_0)]\varepsilon\, d\varepsilon \qquad (6.11)$$

where dE is the energy difference, $\rho(\varepsilon)$ is the density of states of graphene, and f is the Fermi Dirac Distribution function, ε is energy, μ is the chemical potential, and T_e is the electronic temperatures. This integral is split into four separate integrals: two for each temperature - one for the hole side and the other for the electron side. A change of variable is made so that the integral on the hole side is convergent. Solving these integrals yields equation 6.12, where C is the constants from the density of states. k_B is the Boltzmann constant, and Li is a polylogarithmic function. By relating the chemical potential to the interlayer voltage, we can determine the expected profile of the electronic temperature.

$$dE = -\int_{-\infty}^{0} \rho(\varepsilon) f(-\varepsilon+\mu, T_1)\varepsilon\, d\varepsilon + \int_{-\infty}^{0} \rho(\varepsilon) f(-\varepsilon+\mu, T_0)\varepsilon\, d\varepsilon + \int_{0}^{\infty} \rho(\varepsilon) f(\varepsilon-\mu, T_1)\varepsilon\, d\varepsilon - \int_{0}^{\infty} \rho(\varepsilon) f(\varepsilon-\mu, T_0)\varepsilon\, d\varepsilon \tag{6.11}$$

$$\begin{aligned} dE = {} & -2 * C * (k_B T_1)^3\, Li_3\left(-e^{-\frac{\mu}{k_B T_1}}\right) \\ & +2 * C * (k_B T_0)^3\, Li_3\left(-e^{-\frac{\mu}{k_B T_0}}\right) \\ & -2 * C * (k_B T_1)^3\, Li_3\left(-e^{\frac{\mu}{k_B T_1}}\right) \\ & +2 * C * (k_B T_0)^3\, Li_3\left(-e^{\frac{\mu}{k_B T_0}}\right) \end{aligned} \tag{6.12}$$

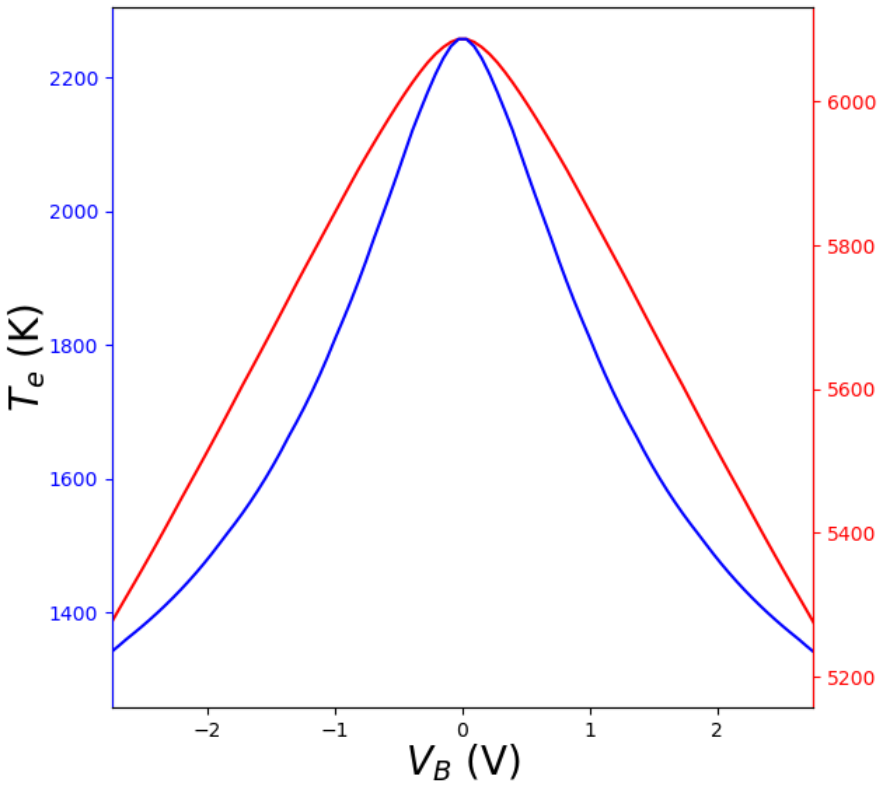

Figure 6.4 Modeled Electronic Temperature. Electronic temperature calculated from the expression in equation 6.12 as a function of interlayer voltage. The red curve has more stored energy than the blue curve (compare the peak electronic temperatures).

The calculated electronic temperature displays a peaked profile symmetric about the Dirac point. This symmetry reflects the symmetry of the electronic heat capacity which depends on the available density of states. Since the density of states is smallest at the Dirac point, the electronic temperature is also expected to be largest. Figure 6.4 shows the calculated electronic temperature as a function of the interlayer voltage based on a generic graphene thermometer device storing two arbitrary amounts of energy, one larger than the other (Red and Blue respectively). We see that at lower energies the electronic temperature profile exhibits a profile more reminiscent of a gaussian profile while at higher energies it is more triangular.

Compared to the calculated electronic temperature the previously extracted electronic temperature profile appears to be a snap shot of the profile as it cools after the initial excitation. As seen in the extracted electronic temperature from a graphene thermometer device, the electronic temperature does not conform purely to either of these shapes. Rather at larger interlayer voltages it is more triangular while closer to the Dirac point it is more of a peak than seen here. This can be explained by the initial fast cooling of the hot carriers. After photoexcitation, the excited charge carriers thermalize almost instantaneously, and are then quickly cooled by optical phonons. Given that the response time of our devices is on the order of 1.5 ps (slower than the initial fast cooling by optical phonons), what we measure is the photocurrent from the remaining still thermalizing population. This suggests that the extracted electronic temperature profile is a snap-shot at the response time of the thermometer (~1.5 ps) of the profile as it cools from a high energy profile after the initial excitation to the low energy one. With the electronic temperature profile established, variations in the profile of this electronic temperature signify new cooling pathways or the increased efficiency of existing ones.

Here in Chapter 6, we have detailed the modeling of the electronic temperature. The electronic temperature we calculated - based on graphene's electronic heat capacity - is in good agreement with the extracted electronic temperature shown in Chapter 5. In Chapter 7, we demonstrate the unusual cooling dynamics of the electron-hole excited states; these dynamics point to cooling enhancements from the formation of a Dirac electron-hole plasma.

REFERENCES

[1] N. Kharche, & S. K. Nayak, Quasiparticle band gap engineering of graphene and graphene on hexagonal boron nitride substrate. Nano Lett. **11,** 5274_5278 (2011).

[2] J. F. Rodriguez-Nieva, M. S. Dresselhaus, L. S. Levitov, Thermionic Emission and negative dI/dV in Photoactive Graphene heterostructures, *Nano Lett.*, 15, 3, 1451–1456 (2015)

CHAPTER 7

Cooling Dynamics of the Dirac Electron-Hole Plasma

7.1 Introduction

Strong thermionic cascade is a direct result of the high electronic temperature, T_e, at the Dirac point. T_e is initially set by the electronic heat capacity of graphene, which is lowest at the Dirac point, thus leads to a large initial T_e. Ultimately T_e is limited by graphene's in-plane heat transfer in graphene. After sufficient time, T_e is expected to reach the bath temperature $T_{lattice}$ via intrinsic momentum conserving collisions at low T and disorder-assisted super-collisions at high $T_{lattice}$ [1,4,6]. As a consequence of the crossover of these two cooling pathways, the electronic temperature after photoexcitation has been shown to exhibit strong *enhancement* at intermediate sample temperatures (T = 50-100 K). As we will show here, the low temperature measurements of the thermionic cascade reveal that the electronic temperature is strongly *quenched* at intermediate temperatures.

7.2 Intralayer Bias and Temperature Dependent Photoresponse

Since the cooling dynamics of the electron-hole excited states involve both interlayer and intralayer effects, the measurement scheme is adjusted to observe any changes in the total photoresponse, which includes its intralayer behavior. This enables us to observe not only the interlayer photocurrent as described in previous chapters, but also the intralayer part, which could contribute to cooling the electron hole excited states. The total photoresponse is measured at different temperatures. At each temperature we apply

an interlayer voltage V_B and a weak intralayer bias voltage V_T between the two contacts of the top graphene layer (Fig. 7.1).

This maps the total photoresponse as a function of V_B and V_T (Figure 7.2). From these photocurrent maps, we removed contributions to the photocurrent that are antisymmetric with respect to V_T (Fig. 7.3) Such contributions include ordinary changes in the in-plane conductivity due to free charge carriers. This is done by summing the photocurrent $I_{PC}(V_B,V_T)$, with the photocurrent $I_{PC}(V_B,-V_T)$. The excess photocurrent that remains after this symmetrization process occurs only across the interlayer barrier yet is sensitive to *in-plane* cooling processes in the top graphene layer.

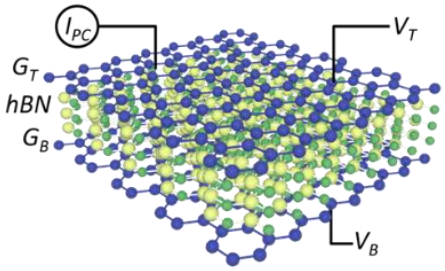

Figure 7.1 Intralayer Photoresponse Measurement Scheme. We simultaneously apply an interlayer voltage, V_B, and an intralayer voltage, V_T, to measure both the interlayer and intralayer response.

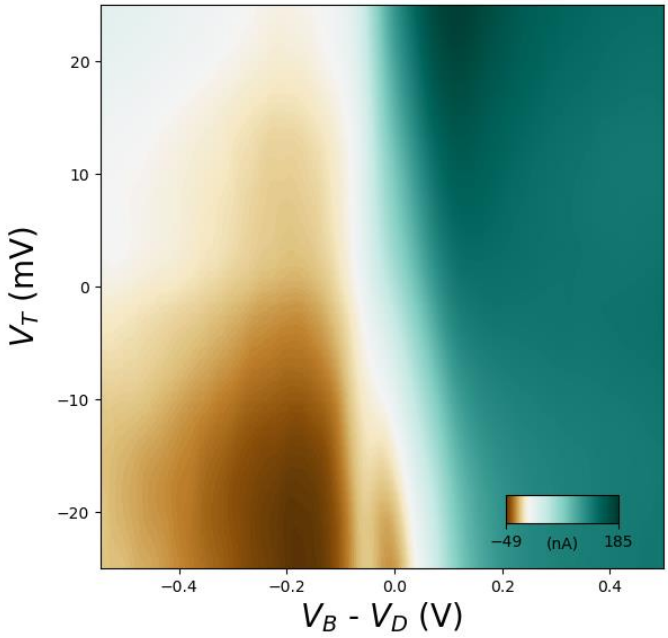

Figure 7.2 Total Photoresponse Mapping. The photocurrent is measured with respect to both interlayer voltage, V_B, and intralayer voltage V_T. The data is centered about the Dirac point voltage V_D.

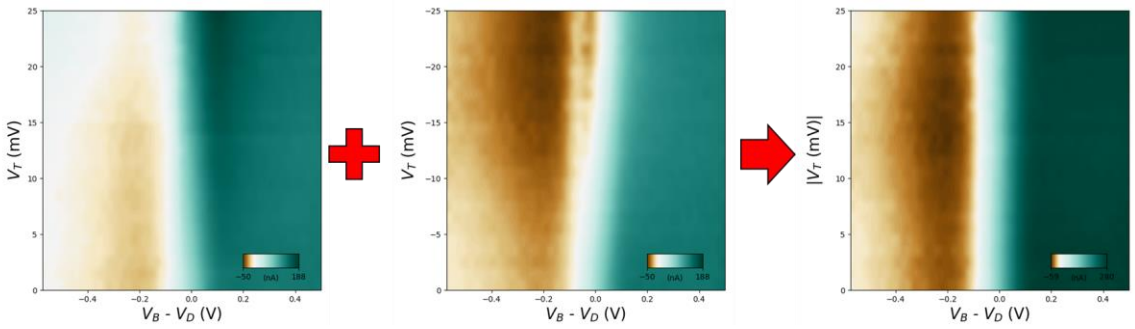

Figure 7.3 Intralayer Data Symmetrization. The changes in photoresponse due purely to the change in free charge carrier density is ignored by summing the data with positive intralayer voltage with its negative counterpart. The resulting data only includes the interlayer photoresponse and any intralayer effects.

Taking the photoconductance, $dI_{PC}/dV_{B,}$ for the symmetrized photocurrent, we once again look for the signatures of the thermionic cascade: its enhancement of the photoconductance. Figure 7.4 compare the photoconductance at two temperatures (T = 143 K and T = 50 K) as a function of V_B and bias voltage V_T. At T = 143 K and above, the photoconductance-voltage characteristics exhibit a single peak that changes weakly with V_T. In strong contrast, at T = 50 K, the photoconductance-voltage characteristics evolve into a prominent multipeaked structure with deep valleys near the Dirac point (Fig. 7.4). The height of the photoconductance peaks increases with temperature and with V_T. Within a narrow region around V_D, the suppression of the photoconductance further transitions into a robust negative differential photoconductance. This quenching of the photoconductance suggest a strong suppression of the thermionic cascade near the Dirac point.

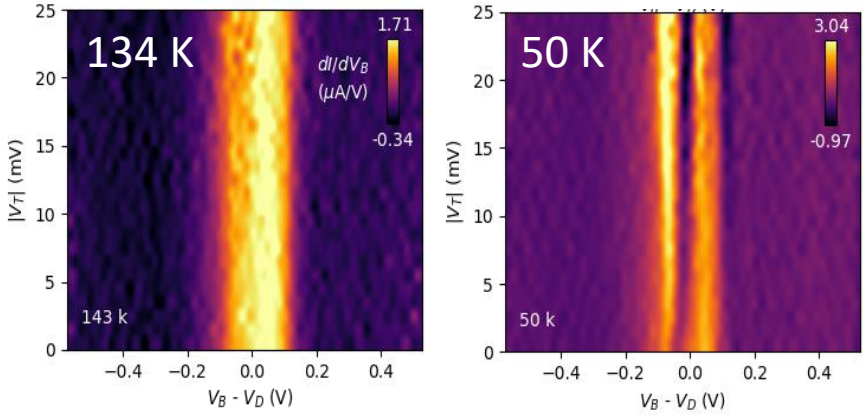

Figure 7.4 Intralayer Voltage and Temperature Dependent Photoconductance. Comparison between 134 K and 50 K photoconductance. Peaks and valleys develop when temperature is lowered and the photoconductance also varies with the magnitude of the intralayer voltage.

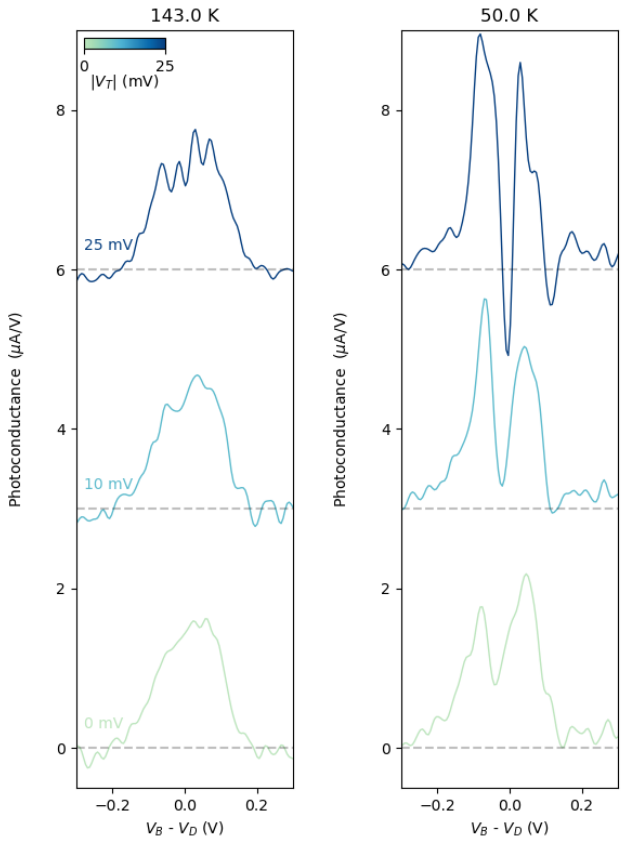

Figure 7.5 Symmetrized Photoconductance Comparison. Comparison between 134 K and 50 K photoconductance at specific magnitude of intralayer voltage. While 143 K shows only slight changes, strong peaks and valleys appears at 50 K and reaches negative differential conductance as intralayer voltage increases.

7.3 Quenching of Thermionic Cascade

The temperature-dependent photoresponse reveals several unique properties of the Dirac electron-hole excited state. As seen in Fig. 7.5, the quenching of the photoconductance occurs with lowering of the lattice temperature and tuning of the intralayer voltage. Since the out-of-plane transit time of cascading carriers is longest near V_D, in-plane thermal conductivity outcompetes interlayer cooling. The excited state population cools rapidly, and the thermionic cascade is quenched. On the other hand, as the chemical potential is tuned away from the Dirac point, the strength of the interlayer electric field increases, which results in positive photoconductance peaks just outside the Dirac region. As V_B is tuned further away from V_D, photoconductance decreases as heating the electron-hole population (and thus the up-conversion of charge carriers) becomes less efficient.

Precisely at the Dirac point, in-plane electrical bias induces extraordinary change in the temperature dependent interlayer photoconductance. We can track the quenching of the excited state by following the photoconductance minima at the Dirac point as we vary interlayer voltage and temperature. As temperature increases (Fig. 7.6a), the Dirac photoconductance at V_T = 25 mV first dips to a minimum at T = 50 K - reaching negative differential photoconductance - before increasing sharply toward room temperature. As shown in Figure 4b, we observe the most pronounced quenching of the interlayer Dirac photoconductance vs. V_T at T = 50 K (Fig. 7.6b).

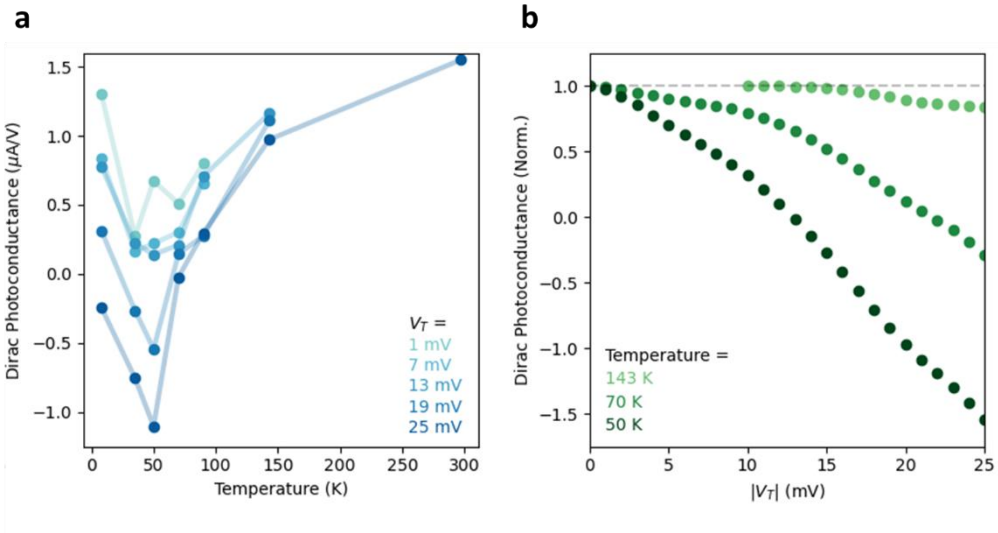

Figure 7.6 Photoconductance Quenching vs Temperature and Intralayer Voltage. The quenching of the photoconductance is sensitive to both temperature and intralayer voltage. The quenching seems to be strongest at intermediately low temperatures around 50 K and at larger values of intralayer voltages.

7.4 Efficient Cooling of Dirac Electron-Hole Plasma

Efficient cooling in the top layer, G_T, gives rise to negative differential photoconductance as charge carriers undergo backflow from the bottom layer. We can visualize the cooling of the system by extracting the electronic temperature as we did previously for the case when V_T = 0 mV at 50 K (Fig. 7.7). The extracted electronic temperature increases as we approach the Dirac point as we might expect from what we saw previously. However, there is now a significant dip, which coincides with the quenching of the photoconductance. Since this electronic temperature is expected to peak at the Dirac point, we can determine the relative cooling by finding the peak-to-valley change of the electronic temperature which comes out to be 325 K. Since our measurement

time window (the relaxation time of the photocurrent) is approximately 1.5 ps, this means that the hot carriers are cooling at a rate of 217 K/ps.

The variations in cooling of the electronic temperature with respect to intralayer voltage and temperature are indicators of at least two separate cooling mechanisms. Suppression of the photoconductance via the intralayer voltage suggests that the in-plane current plays a role in energy relaxation of the carriers; moreover this effect is enhanced at 50 K. This is consistent with the Joule-Thomson process predicted in spatially separate graphene layers [5] in which the coupling of carriers between the two layers mediate in energy relaxation and thus enhances cooling. This, however, does not describe the cooling effects when V_T is absent.

The cooling of charge carriers in the absence of V_T suggests that the cooling is a signature of the Dirac Fluid in graphene. It has been previously predicted that the Dirac liquid phase occurs when carrier-carrier scattering is the dominant interaction for charge carriers in graphene. This has been achieved by suppressing the effects of disorder and phonons via lowering the lattice temperature[3], and by elevating the fermi temperature of the carriers via photoexcitation[2]. In the resulting Dirac Liquid phase, the hydrodynamic drift of carriers further assists in the diffusion of energy of the photoexcited carriers thus cooling the system more efficiently.

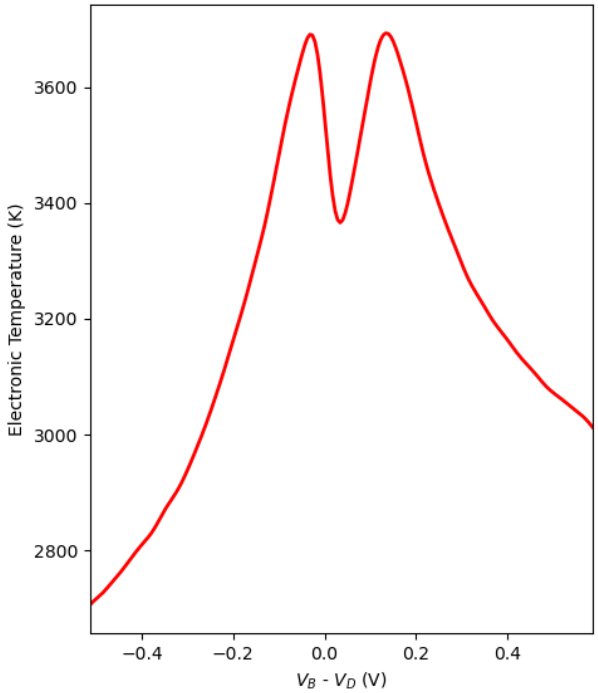

Figure 7.7 Cooling of Dirac e-h Excited State. Plot of the extracted electronic temperature, T_e, as a function of interlayer voltage centered at the Dirac point at 50 K and V_T = 0 V. T_e, shows a dip, which suggests that cooling occurs at the vicinity of the Dirac point unlike in the room temperature case discussed in Chapter 5.

7.5 Evidence of Dirac Electron-Hole Plasma at Room Temperature

In ultraclean devices, we observed a clear suppression of thermionic cascade which indicates the formation of Dirac electron-hole Plasma even at room temperature. While all Graphene/hBN/Graphene devices shown here exhibits hot carrier transit, the efficiency at which this occurs differs between devices. When we compare the room temperature - purely interlayer - photocurrent and photoconductance for the devices listed in Figure 3.12, Device A and Device B exhibit an enhanced photoconductance near the Dirac point, which indicates a thermionic cascade. On the other hand, Device C, being the cleanest device, does not have this feature (Fig 7.8).

The extracted electronic temperature in Device C exhibits efficient cooling indicative of the formation of a Dirac Liquid even at room temperature. When we perform the same calculation to extract the electronic temperature in Device C (Fig 7.9), we see not only an overall significantly smaller electronic temperature but also a dip that develops in the vicinity of the Dirac point. Since the excitation power is similar to that in the other devices, this indicates that efficient cooling occurs in this device even at room temperature. Considering that Device C is the cleanest of the devices, the formation of a Dirac Liquid is possible at room temperature, similar to that seen in Ref. [2]. This could suggest the efficient cooling is a sign of the formation of a Dirac Liquid at room temperature, in which the enhanced diffusive drift of carriers contribute to the spreading of heat thus cooling the electronic temperature. The enhanced diffusion length of a Dirac liquid could also thus suppress the total photocurrent by boosting the hot carriers' ability to exit the active area of our device since the graphene layers extends beyond the overlapping active area. Given that Device C is not only the cleanest, but also has the smallest area of overlap (~30 μm^2) compared to the other two devices (Device B: ~50 μm^2. Device A: ~150 μm^2), the formation of a Dirac liquid would explain the unique behavior of Device C.

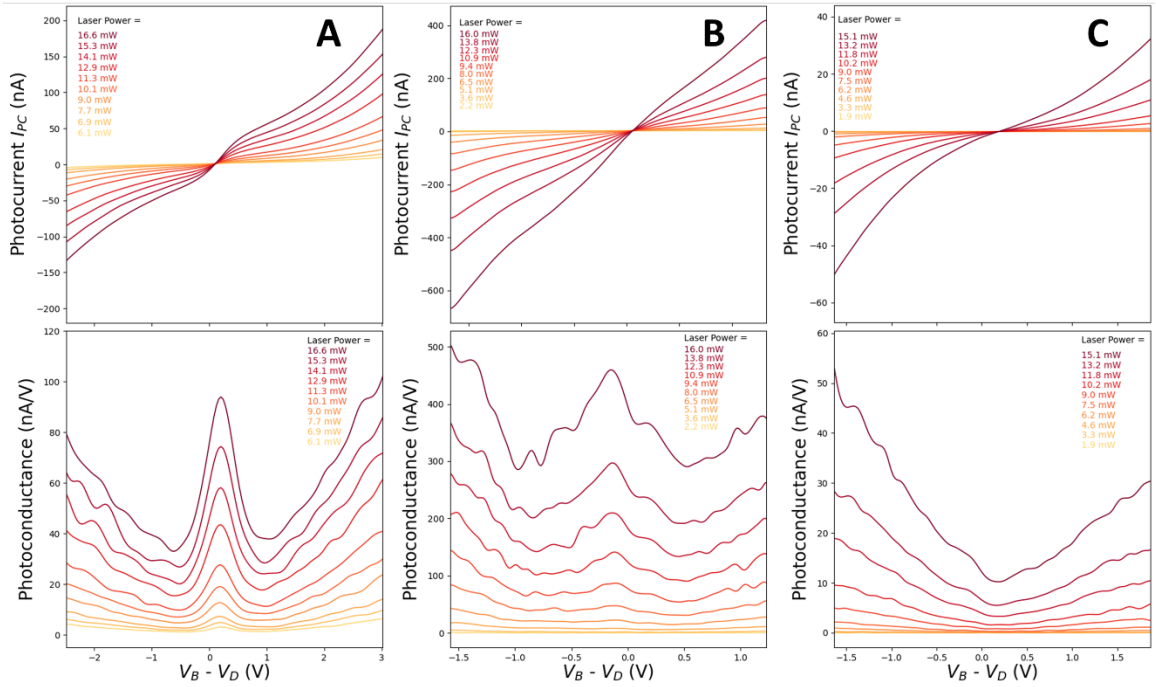

Figure 7.8 Photoresponse Comparisons. Side by side comparison of the photocurrent (top row) for all three devices, and comparison of the photoconductance (bottom bow). The interlayer voltage is offset by the Dirac point voltage, V_D.

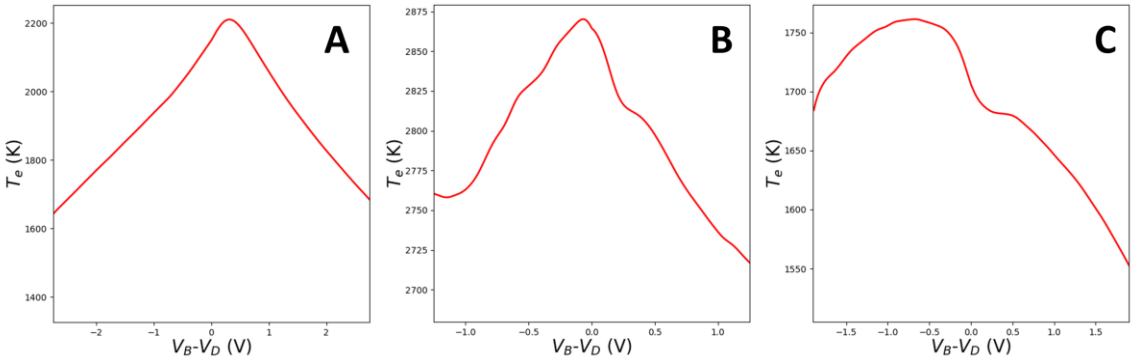

Figure 7.9 Extracted Electronic Temperature Comparison. In an ultraclean device, the Extracted electronic temperature from the room temperature photocurrent data of Device C with 15.1 mW of excitation power shows a developing dip at the Dirac point unlike the other two devices which shows a peak at similar excitation powers of ~15.5 mW.

REFERENCES

[1] A. Betz, S. Jhang, E. Pallecchi, *et al.* Supercollision cooling in undoped graphene. *Nature Phys* **9,** 109–112 (2013).

[2] A. Block, et al., Observation of giant and tunable thermal diffusivity of a Dirac fluid at room temperature, Nature Nanotech. Vol 16 1195-1200, (2021)

[3] J. Crossno, et al., Observation of the Dirac fluid and the breakdown of the Wiedemann-Franz law in graphene, Science, Vol. 351, issue 6277, 1058-1061 (2016)

[4] M. W. Graham, Shi, S-F., Ralph, D. C., Park, J. & McEuen, P, L. Photocurrent measurements of supercollision cooling in graphene. *Nature Phys.* **9**, 103–108 (2013).

[5] J. C. W. Song and Leonid S. Levitov, Energy-Driven Drag at Charge Neutrality in Graphene, Phys. Rev. Lett. 109, 236602, (2012)

[6] J. H. Strait, H. Wang, et. al., Very Slow Cooling Dynamics of Photoexcited Carriers in Graphene Observed by Optical-Pump Terahertz-Probe Spectroscopy, *Nano Lett.*, 11, 11, 4902–4906 (2011)

CHAPTER 8

Conclusions

Here we have demonstrated the tunable infrared photoresponse of a Graphene/hBN/Graphene device; these photoresponse originates from the thermionic cascade of photoexcited hot carriers in graphene. These devices act as a thermometer for the thermalized hot carriers in graphene and are most sensitive near the Dirac point where the up conversion of excited electrons and holes is most efficient. This efficiency is reflected in the peaked electronic temperature near the Dirac point, which leads to a thermionic cascade of excited holes which yields an enhanced interlayer photoconductance. This electronic temperature can be tuned via interlayer voltage, intralayer voltage, and also lattice temperature. At intermediately low lattice temperatures an intensely strong cooling occurs in the vicinity of the Dirac point both, with and without intralayer bias voltage. In the case with intralayer bias voltage, this behavior consistent with an in-plane Joule-Thomson process. This behavior, however, is not possible in cases that lacks intralayer bias voltage, which suggests that the formation of Dirac electron-hole Plasma enhances the carriers' thermal conductivity and leads to efficient cooling. There is also evidence of the formation of this Dirac electron-hole Plasma at room temperature; but only in ultraclean and smaller systems in which scattering with defects and disorder is weak and device maybe smaller than the diffusion length. These optically gated devices also operate on a terahertz timescale similar to an Auston switch. Further studies and theoretical modelling of the precise control of this Dirac plasma may lead to future development of graphene thermionic devices with the high level of control of the hot carrier distribution.